Journal of Volcanology and Geothermal Research 432 (2022) 107672

Contents lists available at ScienceDirect

Journal of Volcanology and Geothermal Research

journal homepage: www.journals.elsevier.com/journal-of-volcanology-and-geothermal-research

A reappraisal of explosive–effusive silicic eruption dynamics: syn-eruptive assembly of lava from the products of cryptic fragmentation

Fabian B. Wadsworth [a,*], Edward W. Llewellin [a], Jonathan M. Castro [b], Hugh Tuffen [c], C. Ian Schipper [d], James E. Gardner [e], Jérémie Vasseur [f], Annabelle Foster [a], David E. Damby [g], Iona M. McIntosh [h], Sina Boettcher [i], Holly E. Unwin [c], Michael J. Heap [j,k], Jamie I. Farquharson [c], Donald B. Dingwell [f], Kayla Iacovino [l], Rebecca Paisley [m], Calvin Jones [d], Jack Whattam [d,n]

[a] Earth Science, Durham University, Science Labs, Durham DL1 3LE, UK
[b] Institute of Geosciences, Johannes Gutenberg Universität, Mainz, Germany
[c] Lancaster Environment Centre, Lancaster University, Lancaster LA1 4YQ, UK
[d] School of Geography, Environment and Earth Sciences, Victoria University of Wellington, PO box 600, Wellington 6140, New Zealand
[e] Department of Geological Sciences, Jackson School of Geosciences, The University of Texas at Austin, Austin, TX 78712-0254, USA
[f] Earth & Environmental Science, Ludwig-Maximilians-Universität, Theresienstrasse 41, 80333 Munich, Germany
[g] U.S. Geological Survey, California Volcano Observatory, 345 Middlefield Rd, Menlo Park, CA 94025, USA
[h] Japan Agency for Marine-Earth Science and Technology (JAMSTEC), 2-15 Natsushima-cho, Yokosuka, Kanagawa 237-0061, Japan
[i] Applied Geology and Environmental Planning, Carl von Ossietzky Universität, 26129 Oldenburg, Germany
[j] Université de Strasbourg, CNRS, Institut Terre et Environnement de Strasbourg, UMR 7063, 5 rue René Descartes, Strasbourg F-67084, France
[k] Institut Universitaire de France (IUF), Paris, France
[l] Jacobs, NASA Johnson Space Center, Houston, TX 77058, USA
[m] Cornish Lithium Ltd, Tremough Innovation Centre, Penryn TR10 9TA, UK
[n] Department of Geosciences, University of Oslo, Sem Sælands vei 1, 0371 Oslo, Norway

ARTICLE INFO

Keywords:
Explosive-effusive transition
Volcanic eruption
Rhyolite
Viscoelasticity
Volcanic outgassing

ABSTRACT

Silicic volcanic eruptions range in style from gently effusive to highly explosive, and may switch style unpredictably during a single eruption. Direct observations of subaerial rhyolitic eruptions (Chaiten 2008, Cordón Caulle 2011–2012, Chile) challenged long-standing paradigms of explosive and effusive eruptive styles and led to the formulation of new models of hybrid activity. However, the processes that govern such hybrid explosive–effusive activity remain poorly understood. Here, we bring together observations of the well-studied 2011–2012 Cordón Caulle eruption with new textural and petrologic data on erupted products, and video and still imagery of the eruption. We infer that all of the activity – explosive, effusive, and hybrid – was fed by explosive fragmentation at depth, and that effusive behaviour arose from sticking and sintering, in the shallow vent region, of the clastic products of deeper, cryptic fragmentation. We use a scaling approach to determine that there is sufficient time available, during emplacement, for diffusive pyroclast degassing and sintering to produce a degassed plug that occludes the shallow conduit, feeding clastogenic, apparently effusive, lava-like deposits. Based on evidence from Cordón Caulle, and from other similar eruptions, we further argue that hybrid explosive–effusive activity is driven by episodic gas-fracking of the occluding lava plug, fed by the underlying pressurized ash- and pyroclast-laden region. The presence of a pressurized pocket of ash-laden gas within the conduit provides a mechanism for generation of harmonic tremor, and for syn-eruptive laccolith intrusion, both of which were features of the Cordón Caulle eruption. We conclude that the cryptic fragmentation models is more consistent with available evidence than the prevailing model for effusion of silicic lava that assume coherent non-fragmental rise of magma from depth to the surface without wholesale explosive fragmentation.

* Corresponding author.
E-mail address: fabian.b.wadsworth@durham.ac.uk (F.B. Wadsworth).

https://doi.org/10.1016/j.jvolgeores.2022.107672
Received 12 May 2022; Received in revised form 8 September 2022; Accepted 12 September 2022
Available online 17 September 2022

1. Introduction

Silicic volcanic eruptions are often divided into those that are vigorously explosive – producing pyroclasts that are widely dispersed by volcanic plumes and density currents – and those that are gently effusive – producing coherent lavas that are emplaced proximal to eruptive vents (Fink, 1983; Eichelberger et al., 1986; Jaupart and Allègre, 1991; Westrich and Eichelberger, 1994; Woods and Koyaguchi, 1994; Dingwell, 1996; Castro and Gardner, 2008; Cassidy et al., 2018). However, individual explosive eruptions can give way to effusive eruptions, transitioning through a hybrid phase in which both eruption styles occur simultaneously (Lara, 2010; Schipper et al., 2013; Castro et al., 2014). Direct observations of the 2011–2012 Cordón Caulle eruption in Chile showed that intermittent explosive activity involving the development of ash-laden plumes can occur *during* sustained lava effusion (Schipper et al., 2013). These observations additionally showed that the explosive jets of gas and pyroclasts are transported to the surface through transient elongate fractures that pervade the effusing lava itself. Similar hybrid activity was seen during the 2008 eruption of Volcán Chaitén (also in Chile), in which an explosive eruption was fracture-fed through the co-erupting lava dome (Pallister et al., 2013; Castro et al., 2014; Heap et al., 2019). In both of these cases, effusion of lava began less than two weeks after the start of the explosive eruption (Castro and Dingwell, 2009; Lara, 2010; Silva Parejas et al., 2012; Castro et al., 2013; Pallister et al., 2013; Schipper et al., 2013). This mixed explosive–effusive eruptive style challenges most existing conceptual models of the shallow subsurface at silicic volcanoes, which cannot account for the simultaneous and quasi-sustained eruption of both fragmental and coherent volcanic products – manifestations of volcanism that imply very different rates of magma ascent and mass eruption rate.

Models for silicic volcanism have had to explain how initial explosive phases produce high-vesicularity pyroclasts that have incompletely degassed, whereas subsequent effusive phases produce coherent lava that is thoroughly degassed. A particular challenge is that the lava bears evidence for having experienced open-system outgassing despite having comparatively low vesicularity. Existing models include (1) a permeable foam collapse model (Eichelberger et al., 1986; Jaupart and Allègre, 1991; Westrich and Eichelberger, 1994; Fink et al., 1992); (2) a fracture-tuffisite model (Castro et al., 2012, 2014; Saubin et al., 2016; Paisley et al., 2019b); and (3) a wholesale fragmentation and re-sintering model (Wadsworth et al., 2020a). However, regardless of whether silicic lava is produced by foam collapse, fracturing, or fragmentation/sintering, the definitive textures associated with magma outgassing are – by definition – healed and overprinted during lava genesis and emplacement. This obscuring of textural history through densification and shear strain during lava emplacement (Gonnermann and Manga, 2005a) is problematic for deciphering the origin of dense silicic lavas and the role played by hybrid eruption styles. Importantly, this means that the clues to lava formation may not be preserved in the lava itself, and that other eruptive products may hold the key to understanding shallow conduit dynamics.

The 2011–2012 Cordón Caulle eruption was well documented, and as such has been invaluable in the recent development of models of silicic eruption dynamics. The generalised conceptual models that have arisen from it (Castro et al., 2014; Wadsworth et al., 2020a; Schipper et al., 2021) have yet to link conduit and other shallow magmatic/intrusive processes with the wide range of observed eruption dynamics, pyroclast and lava textures, and volatile contents of eruption products. Such a model should explain the wealth of complex and highly variable pyroclastic deposits and pyroclast textures at Cordón Caulle within an overarching eruption/emplacement mechanism. It should also reconcile the in-conduit fragmentation processes that are required to produce the observed fine ash, with remote sensing–based interpretations of laccolith intrusion at Cordón Caulle and syn-eruptive geophysical data such as the spatial and temporal evolution of seismicity.

Here, we bring together observations made of the 2011–2012 Cordón Caulle eruption, along with new data for volatile concentrations and textures in pyroclasts, and permeability determinations for the eruptive products, in order to identify the processes at play during explosive, hybrid, and then effusive activity. On the basis of this evidence, we aim to form a holistic conceptual view of the volcanic subsurface that is consistent with the surface observations. We analyse (1) in-vent lava fracture surfaces, (2) volcanic bombs, and (3) centimetric chips of obsidian, all erupted during hybrid activity, and deposited proximally in the pyroclastic cone and surrounding bomb field enclosing all but the north-west side of the vent (Fig. 1). We additionally analyse distal fracture-hosted deposits in the lava. In the context of the wider suite of samples produced during this eruption of Cordón Caulle, and textures reported for other silicic eruptions, we use our new observations to constrain the eruption dynamics that are most consistent with available evidence, discussing the relative contributions and timescales of key processes such as lava assembly and laccolith growth (Tuffen et al., 2013; Castro et al., 2016). We use this case study of a directly observed eruption to produce a general model for explosive–hybrid–effusive that we propose is applicable to similar magnitude explosive eruptions at subaerial silicic volcanoes.

2. Case study: the 2011–2012 eruption of Cordón Caulle, Chile

Cordón Caulle volcano erupted on 4 June 2011 with an initial sub-Plinian phase producing a 9–15 km-high plume (Silva Parejas et al., 2012; Castro et al., 2013; Schipper et al., 2013; Bonadonna et al., 2015). Pyroclastic density currents were generated in the first 10 days of the eruption, with up to 10 km run-out distance, and on 10 June lahars were triggered by rain (Bonadonna et al., 2015; Elissondo et al., 2016). In less than two weeks of the eruption onset, lava began erupting from the same vent while the explosive eruption plume continued (Silva Parejas et al., 2012). Schipper et al. (2013) report a satellite image that shows that, by 3 July 2011, two overlapping pyroclastic cones aligned in a NW-SE direction had formed. By early January 2012, the average plume height was approximately 1.5–5 km. In January 2012, direct video footage was collected from 3.5 km straight-line distance to the vent, looking south-east into a single pyroclastic cone, presumably coalesced from the two overlapping cones. From this direction, both the lava effusion and intermittent gas-and-ash explosive activity could be seen, revealing the fracture-hosted transient conduits opening and closing in the lava pad at the vent area (Schipper et al., 2013). The events documented in those video sequences include (1) effusion of lava with short periods without ash-venting or other phenomena, (2) gas-jetting; (3) ash-and-gas jetting; and (4) Vulcanian blasts producing bombs on ballistic trajectories. Activity moved spatially among up to approximately six locations in the vent area – termed sub-vents (Schipper et al., 2013) – across the whole proximal in-vent lava region, and was temporally unsteady, shifting in activity type (1–4 activity types listed above) over seconds to minutes (Schipper et al., 2013). More video footage taken in February 2012 revealed the same hybrid eruption of both ash-laden plume material during the effusion of lava, with the pyroclastic component of the eruption continuing through and alongside the lava itself. Imagery from these February 2012 videos is introduced in more detail later – supplemented by imagery taken from the same location around a month later – and discussed further in a comparative manner with imagery already presented by Schipper et al. (2013).

The lava effusion proceeded from the lava pad in the vent region within the pyroclastic cone, out through the cone breach in the north-west side, feeding a lava field that extends to the north and the south. Initially, the lava flux was estimated to be >30 m^3s^{-1} (Silva Parejas et al., 2012), waning to 1–10 m^3s^{-1} by January 2012 (Tuffen et al., 2013). While new material appeared to stop erupting from the vent by March 2012, new breakout flows from the flow fronts, lava inflation, and lava morphological evolution continued into early 2013 (Tuffen et al., 2013), due to efficient insulation by the chilled crust. Late-stage flow evolution persisted until cooling finally generated a rheologically stiff

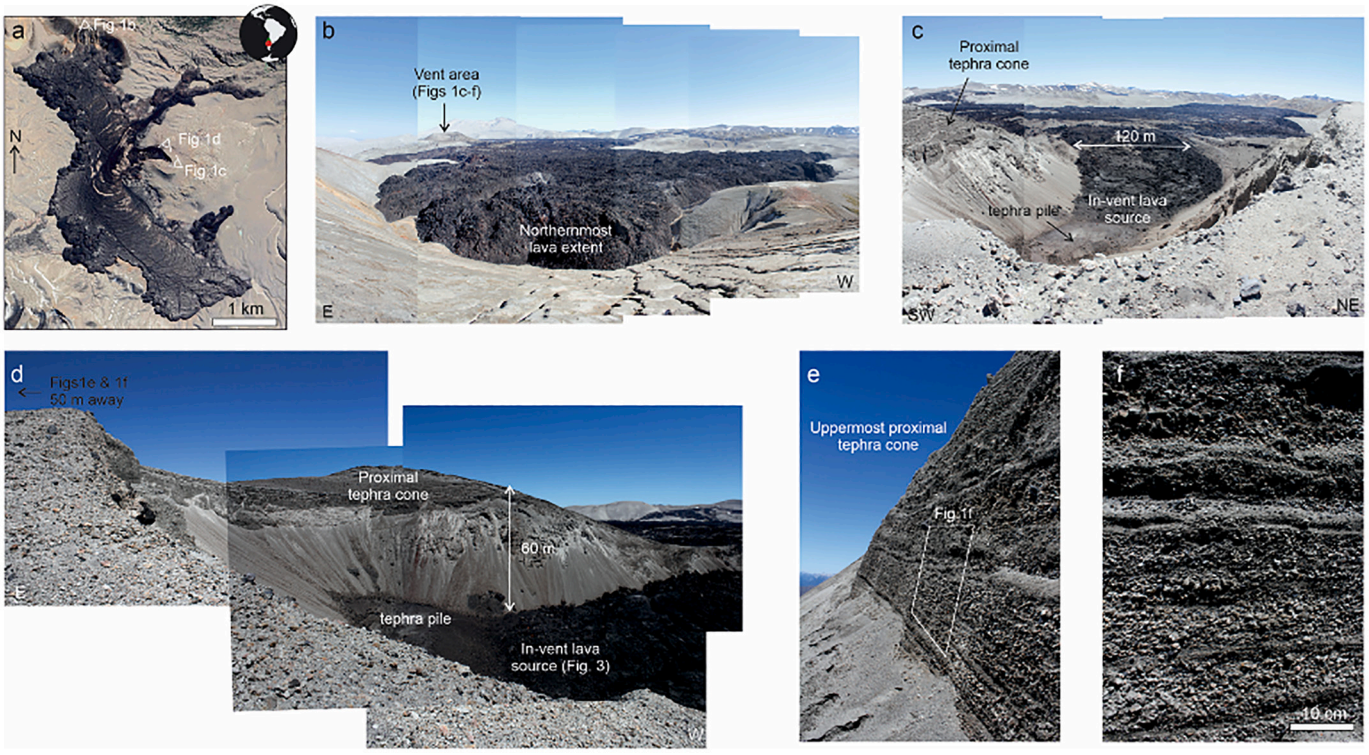

Fig. 1. Broad-scale features at the site of the 2011–2012 Cordón Caulle eruption. (a) Aerial imagery of the vent area showing the extent and morphology of the lava, as well as the vent area (image data ©2019 Google). *Inset*: A globe view of the location of the eruption site in Chile (red dot for location, green arrow for north); the coordinates of the vent are 40 ° 31′22″S, 72 ° 08′55″W. (b) View of the northernmost lava terminus, facing south (vent area indicated). (c) View from the top of the proximal tephra cone looking down and into the vent, showing an in-vent tephra pile at the base of the tephra cone (at the 'back' of the open cone amphitheatre), and the source of the vent-filling lava (see Fig. 3). (d) Side-view of the same features shown in Fig. 1c, showing the structure of the proximal tephra cone. (e) Fall deposits in the uppermost section of the proximal tephra cone. (f) A detail of the same deposits shown in (e). In (b), (c), (d), and (e), a sense of scale is difficult to convey precisely, and so we simply note that the inner lip of the proximal tephra cone is approximately 150 m in diameter and 60–80 m high from the lava surface (see Figs. 1c-d). (For interpretation of the references to colour in this figure legend, the reader is referred to the web version of this article.)

crust sufficiently strong to entirely halt lava advance and inflation (Farquharson et al., 2015; Magnall et al., 2017). The final lava flow thickness, determined from comparing pre- and post-eruptive high-resolution digital elevation models, may have locally exceeded 100 m in parts of the central lava (Delgado et al., 2019), due to infill of a pre-existing topographic depression (Castro et al., 2016). We note that such quantitative thickness estimates would need to account for the uplift caused by the sub-surface laccolith intrusion (Castro et al., 2016), which represents a challenging deconvolution of processes. The total lava volume is 0.4 km^3 (Castro et al., 2016), compared with 1.22 km^3 DRE of tephra from the early explosive phase (4–7 June 2011; Pistolesi et al., 2015; Delgado et al., 2019).

Volcanic bombs that are >0.5 m in diameter were ejected during the hybrid explosive–effusive activity (Fig. 2). These contain complex internal textures (Pistolesi et al., 2015) that indicate they were assembled in the shallow conduit by partial or complete sintering of pyroclastic debris (Schipper et al., 2021) with evidence for gas–pyroclast chemical interactions over timescales of seconds to hours (Paisley et al., 2019b; Heap et al., 2019). Taken together, these constraints suggest that the bombs represent eruption products that capture large-sample snapshots of the heterogeneous in-conduit structure during hybrid explosive–effusive activity. Here, we supplement these observations and modelled timescales with analyses of volcanic bombs and lava from the same eruption, and fine-scale geochemical measurements of obsidian chips from the upper parts of the pyroclastic cone, sampled in January 2014. We synthesise these data to better understand the shallow conduit processes during hybrid activity as a whole.

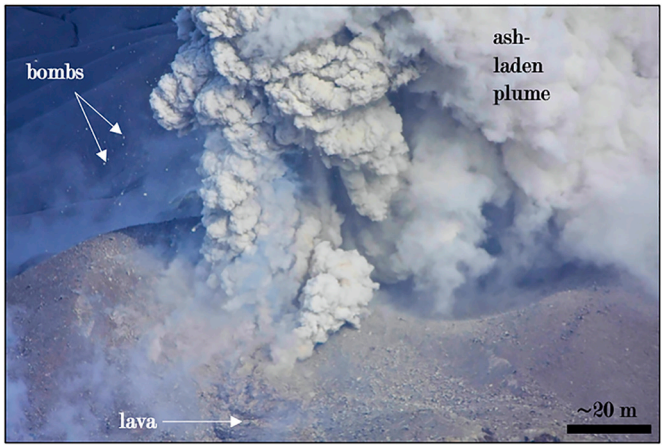

Fig. 2. Hybrid explosive–effusive activity at Cordón Caulle that produced lava, bombs, and an ash-laden plume simultaneously. Photo by Alejandro Sotomayer taken on 14 February 2012. Figure modified after Castro et al. (2014).

3. Materials and methods

In January 2014, fieldwork at Cordón Caulle included work inside the vent area and lava source region enclosed by the pyroclastic tephra cone (Fig. 1) from which the hybrid explosive–effusive eruptions had proceeded two years previously (Schipper et al., 2013). During this field campaign, samples were collected from 4 principal locations: (1) from the internal surfaces of fractures in the lava overlying the vent itself; (2)

from distal lava fronts; (3) from volcanic bombs in cratered areas around the tephra cone; and (4) from vent-proximal fall deposits in the tephra cone walls. Of sample type (4), we collected bulk-samples of the tephra and sub-sampled obsidian pyroclasts – cemtimetric chunks of conspicuous volcanic glass in among the lapilli tuff fall deposit. From bulk samples of the fall deposits, we sub-sampled 16 of the dense obsidian pyroclasts from the upper cone deposits, mounting them in epoxy and polishing the set stub down until the pyroclasts were exposed across their equator. We also doubly polished wafers of some samples for analysis of H_2O concentrations (see Section 3b) and these doubly polished wafers were additionally used for image analysis. Lava samples far from the lava fracture surfaces (sample type (1) above) are not analysed herein because extensive shear strain during emplacement and flow overprints textures.

3.1. Scanning electron microscopy

We employ electron scanning microscopy to image the sample textures and energy-dispersive X-ray analysis for some detailed compositional information of sub-micron features (discussed later). Obsidian pyroclasts were imaged with backscattered electron mode (BSE) on a Tescan Vega 3 variable-pressure scanning electron microscope (SEM), and elemental maps produced using two integrated 150 mm^2 Oxford X^{max} energy-dispersive X-ray (EDX) detectors. Analyses were performed with a beam voltage of 15 kV and a working distance of 15 mm. Maps were collected at a resolution of 1024 × 1024 pixels per image, and pixel dwell time of 100 μs. Using samples of the internal surface of fractures in the in-vent lava deposits, we imaged fracture surfaces, without cutting or polishing, using oriented mounts of the surface itself. These were analysed using a Philips XL30 tungsten filament SEM with identical working conditions to those used with the Tescan Vega 3.

3.2. Fourier transform infrared spectroscopy (FTIR)

Samples for FTIR analysis were prepared as parallel-polished free-standing wafers of known thickness. Imaging FTIR analyses were conducted at JAMSTEC using a Varian FTS Stingray 7000 Micro Imager Analyzer spectrometer under N_2 gas purge with an attached UMA 600 microscope (McIntosh et al., 2014). Images were collected in transmission mode in the mid-IR range (6000–700 cm^{-1}) over 512 scans at a spectral resolution of 8 cm^{-1} using a ceramic (globar) infrared source, a Ge-coated KBr beamsplitter, and a liquid nitrogen-cooled Varian Inc. Lancer Focal Plane Array (FPA) camera housed in the microscope. The FPA camera consists of 4096 infrared photovoltaic $HgCdTe_2$ (MCT) detector pixels arranged in a 64 × 64 grid that image a 350 × 350 μm sample area, producing an IR absorbance image with a pixel spatial resolution of ~5.5 × 5.5 μm. Additional transmission spot analyses covering the near-IR range were conducted using a standard liquid nitrogen-cooled $HgCdTe_2$ (MCT) detector attached to the same spectrometer system (McIntosh et al., 2017), with spectra collected over 512 scans at a spectral resolution of 8 cm^{-1} with a spot size of 20 × 20 μm.

Images and individual spectra were processed using the Varian Win-IR Pro software (v3.3.1.014). All volatile absorbance values were measured as peak height above a linear baseline, which can be converted into concentration data by entering absorbance, glass density, glass thickness and peak-dependent molar absorptivity coefficient values into the Beer-Lambert law (Stolper, 1982). A glass density value of 2374 kgm^{-3} was used for all spectra (iterated). Sample thickness was measured by digital micrometer with a precision of ±1 μm local to the spot measurements taken. Samples CC1, CC3 and CC4 were 466, 480, and 120 μm thick, respectively. The mid-IR 1630 cm^{-1} H_2O_m absorbance peak was not observed (i.e. was below the detection limit) for sample CC3; for the thicker CC1 and CC2 samples the entire <2000 cm^{-1} region was oversaturated due to absorption related to the silicate network so the near-IR 5200 cm^{-1} H_2O_m absorbance peak was checked and also found to be below the detection limit. The 3500 cm^{-1} H_2O_t absorbance peak requires a molar absorptivity coefficient ε that varies according to the proportions of H_2O_m and OH dissolved in the glass (Newman et al., 1986). If rhyolite glass contains no H_2O_m, $\varepsilon3500 = 100 \pm 2$ $lmol^{-1}cm^{-1}$. To constrain how the value of ε3500, hence calculated H_2O_t concentrations, might be affected by undetected H_2O_m, the maximum possible concentration of undetected H_2O_m was calculated for each sample by inputting the 0.005 absorbance detection limit into the Beer-Lambert law with ε5200 value of 1.75 ± 0.08 $lmol^{-1}cm^{-1}$ (Okumura and Nakashima, 2005) or ε1630 value of 55 ± 2 $lmol^{-1}cm^{-1}$ (Newman et al. 1986). These H_2O_m wt% values were then used in a modified Beer-Lambert law method (McIntosh et al., 2017), which accounts for the species-dependence of the ε3500 value. The H_2O_m detection limit is 0.05, 0.05 and 0.01 wt% for samples CC1, CC3 and CC4, respectively, corresponding to lower ε3500 limits of 80, 86 and 98 $lmol^{-1}$ cm^{-1}. However, using these lower ε3500 limits would only increase H_2O_t by 0.00–0.02 wt%. All H_2O_t concentration data were therefore calculated using $\varepsilon3500 = 100$ $lmol^{-1}cm^{-1}$. The 2350 cm^{-1} CO_2 absorbance peak was also below detection in all samples. Using a ε2350 value of 1214 $lmol^{-1}cm^{-1}$ (Behrens et al., 2004) this corresponds to CO_2 detection limits of 2–6 ppm.

In addition to the imaging FTIR measurements described above, we also performed spot measurements using a dry-nitrogen purged Thermo-Nicolet FTIR Bench with attached continuum microscope. Spectra were collected on aperture-constrained spots of ~25 to 50 μm diameter, in transmission mode, and at a spectral resolution of 4 cm^{-1}. Measurements utilised 256 scans, however some experiments with 512 scans were needed for particularly thick, dark samples. Sample-free-path background spectra were collected every 30 min and subtracted automatically from successive unknown sample spectra to mitigate the detection of atmospheric CO_2 and provide absorbance-based spectra that could be readily quantified via the Beer-Lambert Law. For these measurements we used $\varepsilon3500 = 80$ $lmol^{-1}cm^{-1}$. As noted above, this choice of ε3500, rather than using 100 $lmol^{-1}cm^{-1}$ confers an uncertainty on the total water measurement, such that for samples with 0.1 wt% H_2O, the uncertainty is ≲0.02 wt% and for the end-member case of a sample with 0.5 wt% H_2O, this uncertainty is ≲0.1 wt%. These uncertainties, and the associated repeatability uncertainty (which is much smaller), are quoted along with the data, when they are presented in Section 6. As with focal plane array analysis, no magmatic CO_2 was detected.

3.3. Thermogravimetric analysis

Whereas the volatile concentrations remnant in the obsidian chips can be determined quantitatively by FTIR (Section 3b), the volatile concentrations in the material captured on the lava fracture surfaces in the vent-filling lava cannot, because the fragility of the surface veneering made sample wafer preparation difficult or impossible. Therefore, for those samples, we used a Netzsch® Pegasus 404C simultaneous thermal analyzer, which measures the change in mass and internal heat flow of samples during heating and cooling treatments. First, we dried the samples at 190 °C for 48 h, to remove adsorbed H_2O. Here, we exclusively utilise the mass change determinations wherein total mass loss on heating is taken to be a proxy for the total volatile mass that is excess to the solubility up to the maximum temperature used (Giachetti et al., 2015; Shields et al., 2016). We loaded ~90 mg of sample into a platinum cup, and used a 0.17 Ks^{-1} (10 $Kmin^{-1}$) heating and cooling rate, applied linearly up to 1673 K in an argon atmosphere to avoid oxidation. The total mass loss was recorded. For these measurements, we assume that total H_2O is the dominant species controlling the mass loss. In this case, the solubility conditions of relevance are equivalent to the peak experimental temperature and an H_2O partial pressure at the laboratory furnace conditions of 0.2–0.4 bar (von Aulock et al., 2017; Wadsworth et al., 2019). Under these conditions, the Liu et al. (2005) model predicts an H_2O solubility of 0.03–0.05 wt.%, such that here we add 0.04 wt.% to the values we measure and acknowledge an

uncertainty on this approach of ±0.02 wt.%.

3.4. Laboratory determination of permeability of lava fracture surfaces

We measured the permeability of the lava fracture surfaces. A 20 mm-diameter cylindrical sample was cored from a block of the lava containing a fracture surface with a thin, red-coloured veneer (sample length ~ 27 mm). The core was prepared such that its axis was perpendicular to the fracture surface. The end face without the veneer was precision-ground flat and perpendicular to the sample axis. The sample was first inserted into a rubber jacket. Glass beads (1 mm in diameter) were poured inside the jacket at the end of the sample with the thin veneer and a metal endcap (5 mm-thick) containing a 1 mm-diameter hole and a pore distribution plate was placed over the bead layer. The sample assembly was then inserted into a benchtop steady-state permeameter. The confining pressure was set at 1 MPa. The layer of glass beads (about 10 mm in thickness) ensured that the end face with the veneer was flat and perpendicular to the sample axis, a prerequisite for permeability measurement in the laboratory. It was assumed that the permeability of the glass bead layer is considerably larger than that of the sample such that its influence on the measured permeability can be neglected. For the sample as-collected (i.e. with the veneer on it), the steady state volumetric flow rate Q – which is required to determine the permeability – was below detection limits. In order to compare this with the permeability of the lava without the veneer, the adhered sintered fracture surface veneer was ground off from the sample, and the permeability measurement was repeated. In this case, the steady state volumetric flow rate Q of nitrogen could be measured and was recorded using a gas flow meter under an applied gas pressure gradient. At steady state, the permeability k can be found from a suite of measurements of Q using Darcy's law $Q = -kA \nabla P/\mu$, where μ is the viscosity of nitrogen, A is the sample cylinder area, and ∇P is the average applied pressure gradient. For compressible gas, $\nabla P = (P_d^2 - P_u^2)/(2LP_d)$ where P_d is the downstream (atmospheric pressure), P_u is the upstream applied gas pressure, and L is the sample length (Kushnir et al., 2017). Measurements of $Q(\nabla P)$ were made in the linear Darcian regime (Heap et al., 2017; Wadsworth et al., 2020b).

4. Field observations made in January 2014

4.1. Observations from the proximal fall deposits in the vent area tephra cone

The vent area is defined by a west-facing tephra cone amphitheatre (60–80 m tall measured from the lava surface; Figs. 1a-d), from which the lava emanates, and from which the intermittent hybrid plumes and volcanic bombs were erupted (Fig. 2; Schipper et al., 2013). The uppermost tephra cone is accessible from the top and is dominantly constructed from pumice lapilli-tuff fall deposits (Figs. 1e-f) and intermittent bombs (with associated bomb sags). The uppermost cone deposits (Figs. 1e-f) sampled here are assumed to be approximately associated with the late or final fall deposits to be emplaced during hybrid activity (phase 3 in the stratigraphy of Pistolesi et al. (2015)). The cone deposits are a well-sorted, clast-supported, lapilli-tuff fall deposit, comprising on average pumice lapilli and ash (~90 vol.%), lithics (~5 vol.%), and obsidian pyroclasts (~5 vol.%). The componentry varies vertically and laterally over meter scales with obsidian pyroclasts locally reaching up to 20 vol.%. A broad, domed tephra pile is at the inner cone floor, surrounded and topped by larger lava bombs and blocks (Fig. 1c-d). This in-vent tephra pile onlaps with the tephra cone, and therefore post-dates the tephra cone itself – this tephra pile appears to be directly associated with the explosive venting component of the hybrid behaviour.

4.2. Field observations of the 2011–2012 lava

A tongue of lava extends westward from the cone, feeding the main body of the lava (Fig. 1c), which then splits into lobes that extend to the north and south (Fig. 1a). The most proximal-to-source, in-vent lava hosts open, smooth-walled fracture surfaces that have a red veneer (Fig. 3a-c). The red veneer fades upward over several meters in regions where the fractures extend vertically and approach the lava surface (Farquharson et al., 2022). Superimposed on the red veneer are fused angular chunks of lava-like material (~1.5 cm), and the veneer itself appears almost fluidal in texture with lineations along a preferred, broadly upward direction in places (Fig. 3a).

Comparison of the in-vent lava fracture surfaces (Figs. 3a-c) with fractures in the more distal lava (e.g. Fig. 1b), reveals key similarities. Open fractures in the distal lava also have red-coloured veneers (e.g. Fig. 3d), however, compared with the veneers in the in-vent lava (millimetric), the veneers in the distal lava are on average much thicker (centimetric; Fig. 3d). Additionally, in the distal lava, the red veneers grade into polymict pyroclastic fracture fill that is variably welded or entirely un-welded and granular (Figs. 3d-f). The pyroclastic fracture fill is composed of orange-coloured pumice lapilli and ash, obsidian pyroclasts, fragments of lava, and rare lithics. In some cases where the immediate surface of the lava fracture is visible through eroded gaps in the pyroclastic fracture fill, there is evidence for a high shear strain vesicular zone, similar in texture to tube pumice (Figs. 3f-g). In all cases, the shear strain is vertical or sub-vertical. The red veneer is not always present and in some cases the lava is in direct contact with the pyroclastic fracture fill (e.g. Figs. 3e & 2h), or there is a black glassy selvedge between the lava and the pyroclastic fill. Where the fracture surfaces are undulous, the degree of particle sintering is variable (Fig. 3h). In some cases, the pseudo-tube pumice texture occurs in contact with the red veneer material and shows that the shear deformation has incorporated some of the veneer material itself (Fig. 3i).

4.3. Observations from volcanic bombs ejected during hybrid activity

Volcanic bombs erupted during the hybrid explosive–effusive phase of activity demonstrate a wide range in textures (Paisley et al., 2019b; Heap et al., 2019; Schipper et al., 2021). We document some key examples that are representative of the textures found in bombs deposited around the lava deposits (see Fig. 2a in Schipper et al. (2021) for bomb distribution around the vent). The complexity and variety of bomb textures led to them being grouped as 'composite bombs' (Schipper et al., 2021). However, some broad classification is useful here: (1) bombs that are composed of poorly- to moderately-sintered tuff with variably rounded matrix-supported clasts of pumice and lithics in an ash-rich matrix; (2) dense lava-like and obsidian-dominated bombs that frequently contain pumice clasts or are juxtaposed at sharp textural boundaries with welded pumice lapilli and ash tuff; (3) breadcrust bombs which appear to be inflated versions of either type (1) or type (2); and (4) bombs hosting centimetre-scale thicknesses of finely laminated and crossbedded volcanic ash deposits in fractures, or internal to pumiceous pore spaces (Fig. 3). By documenting bomb types around the vent area, it is clear that type (1) bombs are the most common, and that within type (1) there occur variants including variable oxidation and variable evidence for shear deformation and degree of sintering (see Fig. 4 for a broad overview of bomb types present).

5. SEM-based micro-textures of eruptive products

Using the same divisions between (i) fall deposits, (ii) lava deposits, and (iii) bombs, as used in Section 4, we present here the results of SEM-based micro-textural observations. For the fall deposits, we focus exclusively on the textures internal to the obsidian pyroclasts (Section 4a), presenting novel observations of their microstructures.

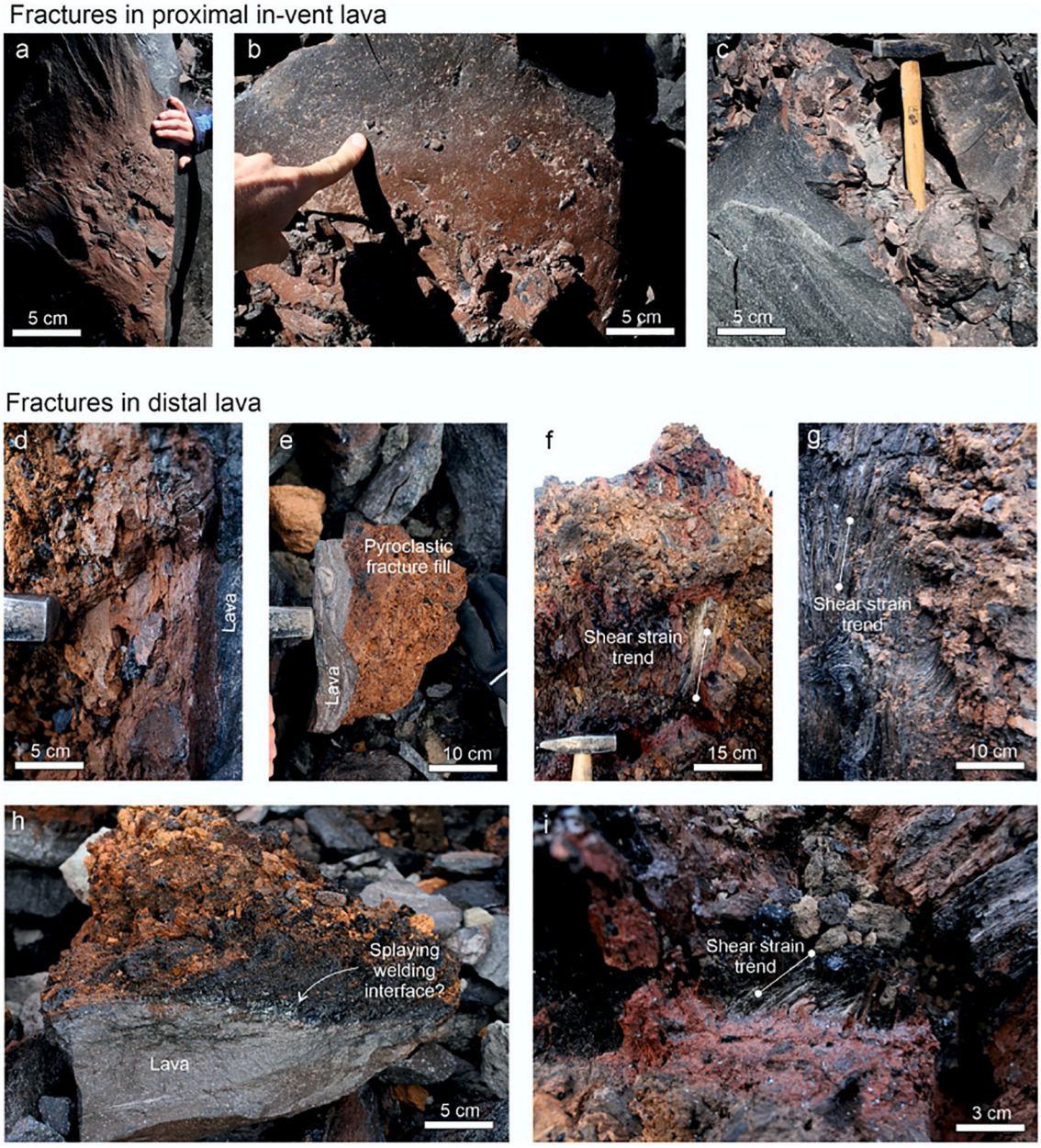

Fig. 3. Key textural features found in the 2011–2012 lava produced during hybrid eruptive activity. Lava (a-c) inside the vent area (see Figs. 1c & 1d) at the lava source or (d-i) at the flow-front (see Fig. 1b). (a-b) Surface of wide open in-vent lava fracture surfaces coated with a red veneer and occasional adhered clasts and sub-vertical fluidal wisps. (c) Similar feature to (b), but showing where the red veneer occurs in complex lava fractures containing brecciated lava blocks. (d-e) Transition from lava fracture surface to pyroclastic fracture fill; in (d) this is gradational through a sheared, dark red zone, whereas in (e) this is sharp. (f) Polymict adhered pyroclastic fracture fill viewed normal to an open lava fracture surface, and showing high shear strain vesicles with a sub-vertical trend (details in (g) and (i)). (g) Detail of the vesicle shear strain texture on the lava fracture surface itself. (h) Loose block of the interface between the lava and the pyroclastic fracture fill with a sintering degree associated with the curved lava surface. (i) Detail of the vesicle shear strain texture but here not associated with the lava surface itself, and instead transitional with a deposit of thoroughly welded pyroclasts within the fracture-fill. (For interpretation of the references to colour in this figure legend, the reader is referred to the web version of this article.)

5.1. Obsidian pyroclasts from fall deposits in the tephra cone

The textures of the obsidian pyroclasts preserved in the tephra cone surrounding the vent are variable in terms of local crystallinity (mineralogy and phenocryst phase proportions), vesicularity (vesicle number density, size distribution, and morphology), and the proportion of groundmass glass. Here, we present an overview of representative textures from sampled obsidian pyroclasts (Fig. 5).

First, we find evidence for unconformable planar features that juxtapose two textural regimes (Figs. 5a & 5b). These planar features are sharp, and truncate groundmass flow bands (Fig. 5b), groundmass crystal textures, and phenocrysts (Figs. 5a & 5b). In all cases, one textural regime (on one side of the planar feature) is vesicle-poor, and contains flow bands and phenocrysts, the second textural regime (on the other side of the planar feature) is aphyric but vesicular. The planar feature contacts are often associated with a bright crystal phase at the boundary itself (e.g. Fig. 5a). The aphyric and vesicular textural regime is always at the edge of the obsidian pyroclast. In the same obsidian pyroclasts as those with the planar features, we find evidence for in-phenocryst glass-inclusion rupture (Fig. 5c).

Fig. 4. Volcanic bombs associated with hybrid eruptive behaviour. (a) Bomb composed of poorly welded pumice clasts in an ash-dominated matrix. (b) Bomb composed of moderately welded pumice clasts with a shear fabric and poorly developed banding, with ash-dominated matrix. (c) Intermediate between the bomb in (a) and the bomb in (b), showing some evidence of shear strain. (d) Bomb with pumiceous domains juxtaposed with red oxidised ash-dominated domains with some splay-and-fade sedimentary structures. (e) Example of a bomb composed of poorly welded polymict clasts of obsidian and pumice in a matrix of ash. (f) Rare dense obsidian bomb. (g) Moderately welded bomb of pumice clasts with a prominent obsidian clast welded in (reproduced with permission from Schipper et al., 2021). (h) Bomb with flow-banded dense obsidian juxtaposed with welded pumice clasts in a matrix of ash with a poorly developed fabric in the welded pumice sub-parallel to the sharp interface with the obsidian. (i) Multiple fragments of a large bomb composed of flattened pumice in an ash matrix with a well-developed shear fabric. (j-l) Examples of cut samples through bombs similar to the example shown in (d), all with sedimentary structures and evidence for variable sintering (images in (j) and (k) are reproduced with permission from Paisley et al. (2019a)). (j) Bounded ash-filled vein with sedimentary structures between two domains of pumice with evidence for pumice densification on the margins of the vein. (k) Sedimentary structures in ash-filled fractures within a pumiceous bomb, including the incorporation of obsidian pyroclasts. (l) Obsidian pyroclasts in a matrix of sintered volcanic ash, together forming a bomb. (For interpretation of the references to colour in this figure legend, the reader is referred to the web version of this article.)

Next, we find obsidian pyroclasts, with low crystallinity and vesicularity, that contain isolated, sub-rounded to sub-angular domains of locally high groundmass crystallinity and vesicularity (Fig. 5d). The boundaries of these internal domains, which are marked by a sudden change in groundmass crystallinity, are not planar, and may be highly convoluted (Fig. 5e). The vesicularity in the internal domains is characterised by convolute and complex vesicle morphologies with some vesicle connectivity over short (~100 μm) length scales. Those internal domains themselves contain sub-domains of glass that is less dense than the surrounding groundmass (Fig. 5f). We find internally pumiceous ash-sized fragments set in the groundmass of the obsidian pyroclasts. These fragments are usually rounded to sub-rounded and approximately 10–30 μm in equivalent spherical radius (Figs. 5g-i). The fragments are often themselves in a matrix of non-vesicular aphyric glass, which is set in the flow-banded groundmass of the obsidian pyroclasts (Fig. 5i). There is some evidence that the microlites in the groundmass of the obsidian pyroclast align with the fragments close to their boundaries, apparently deflecting from the orientation of the flow bands in the obsidian pyroclasts (Fig. 5g). As with the planar features (Figs. 5a & 5b), the boundaries of these fragments are often associated with a bright (high relative

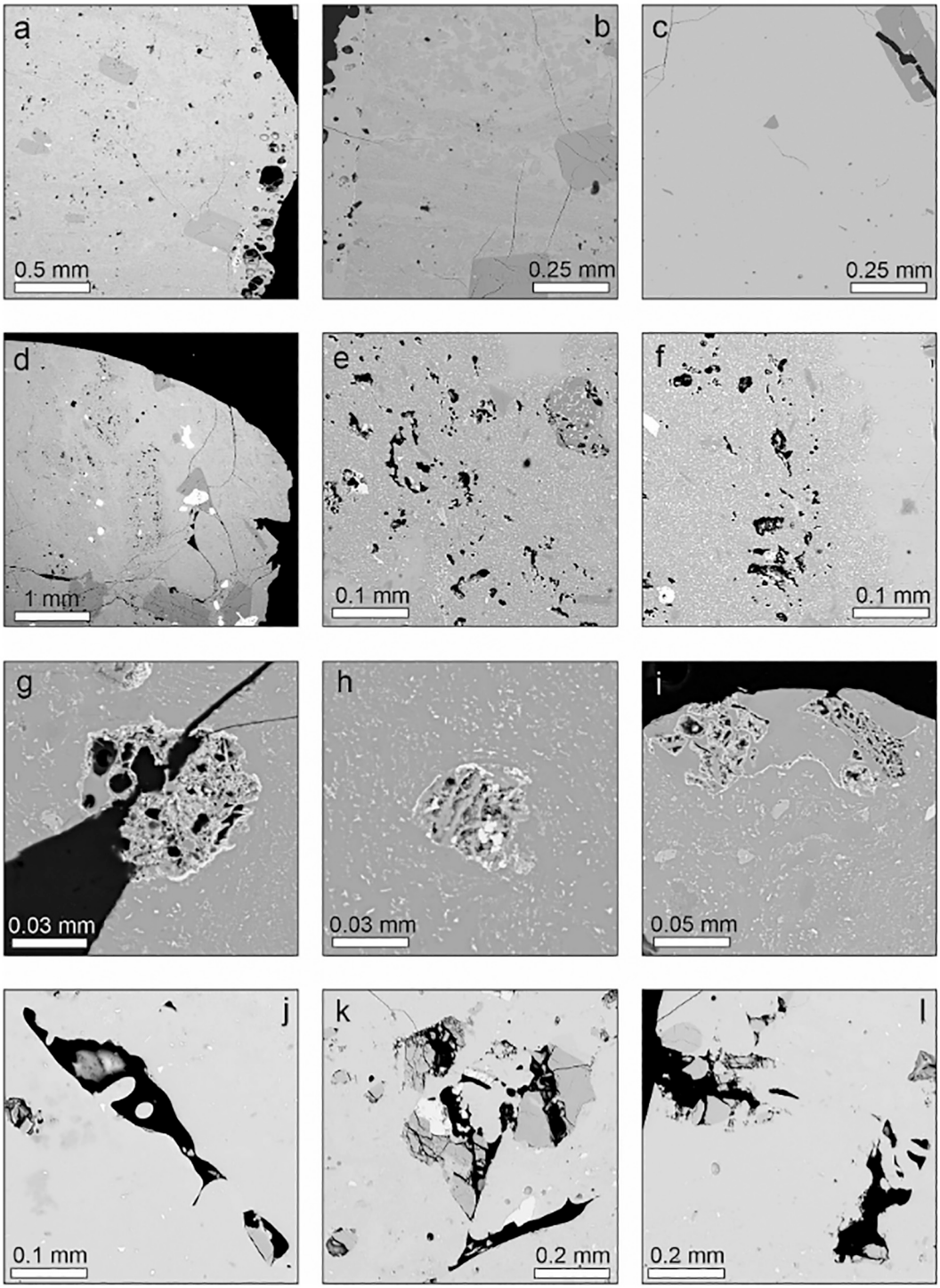

Fig. 5. Internal textures of the obsidian pyroclasts from hybrid eruptive behaviour. (a) and (b) show evidence for a healed fracture juxtaposing texturally distinct domains. In (a) the juxtaposition is between poorly vesicular, crystal-bearing glass (left) and aphyric vesicular glass (right). In (b) the juxtaposition is the same as in (a) but reversed (we note that in (b) the crystal-bearing glass is flow-banded). (c) Approximately mode-1 crystal fracture in the hot state, such that glass filaments connect both sides of the crystal. (d) Porous and microcrystalline domains in the groundmass glass of a less crystalline obsidian chip. (e-f) Fine scale structure of the porous domains shown in (d). (g-i) Full inclusion of porous volcanic ash particles internal to the obsidian pyroclasts. (j-l) Textural evidence for incomplete sintering including the quenched unrelaxed remnants of particle boundaries and bulbous partially sintered glass particles internal to pore spaces.

density) crystalline phase.

In obsidian pyroclasts that are aphyric, we find evidence for cuspate lips at the boundaries with larger (100–300 μm) elongate pore spaces (Fig. 5j-l). These cuspate lips are often associated with rounded protrusions in the pore spaces (Fig. 5j), or curvi-planar pore walls in concave morphologies.

In Fig. 5, some of the obsidian flow-banding (Figs. 5a & 5b) and groundmass texture (Fig. 5i) is associated with groundmass wisps of microlites. Examining these features in more detail, we find evidence for wisps of aligned bright (high relative density) microlites in domains that grade into aphyric domains within the same pyroclast (Figs. 6a & 6b). In some cases, the wisps are linear and begin and terminate in the

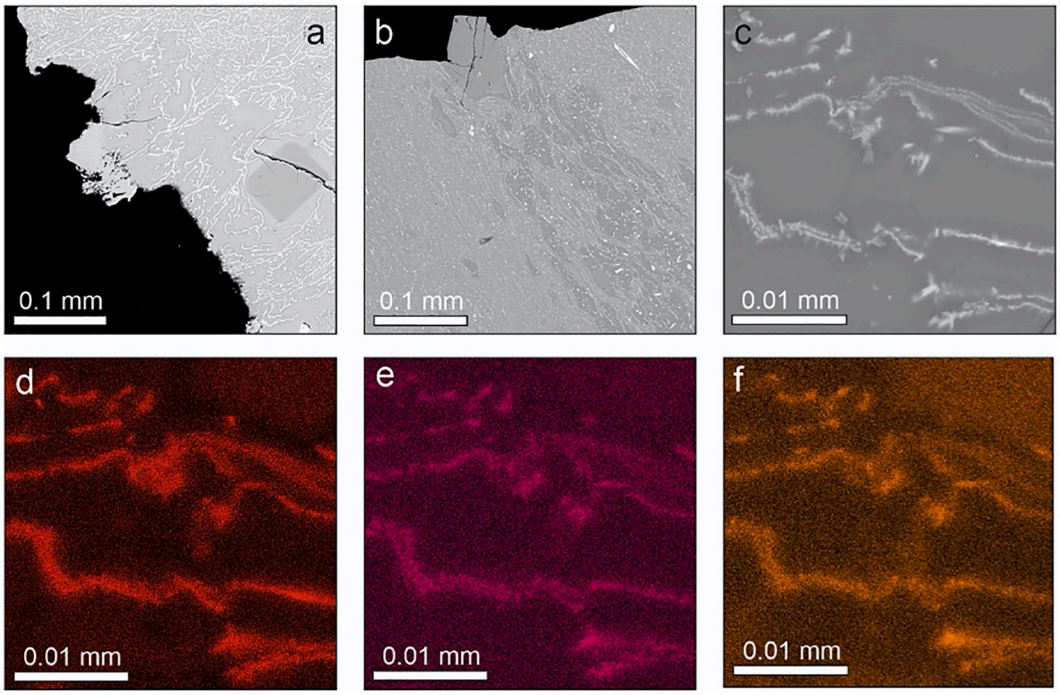

Fig. 6. Groundmass textures in obsidian pyroclasts showing details of the wisp-like crystalline sutures that pick out relict particle boundaries (a-c). (d-f) EDX point maps of the same region given in (c), for which the elements displayed are (d) Fe, (e) Mg, and (f) Ca.

groundmass glass, but in other cases, they connect in a curvi-planar loop and do not terminate in the glass, instead enclosing regions of glass (Fig. 6a). In detail, these wisps occur as linear features, but associated with microlites that have grown into the glass either side of the wisp-trail (Fig. 6c). EDX analyses demonstrate the wisps to be elevated in Ca, Mg, and Fe (and not substantially in any other element), relative to the surrounding glass. Conclusive mineral phase identification was not possible due to the fine scale of these wisps (<1 μm widths, while SEM images typically irradiate sample depths of 1–2 μm), but the observed cationic enrichments are consistent with them being clinopyroxene (Figs. 6d-f). We acknowledge that the backscatter grayscale intensity would also be consistent with Fe-Ti oxide phases. However, clinopyroxene has been identified as part of the 2011–2012 Cordón Caulle eruption petrology (Castro et al., 2013) and is ubiquitous in other rhyolites (Castro and Gardner, 2008). In the same obsidian pyroclasts that contain microlite wisps, there is often evidence for pore-filling vapour-phase mineralization (Figs. 7a & 7b), with evidence for foam-like domains in the glass bordering the pore space, and prismatic silica-dominated crystals in the pore space itself (identified as cristobalite using the textural habit, following Damby (2012)).

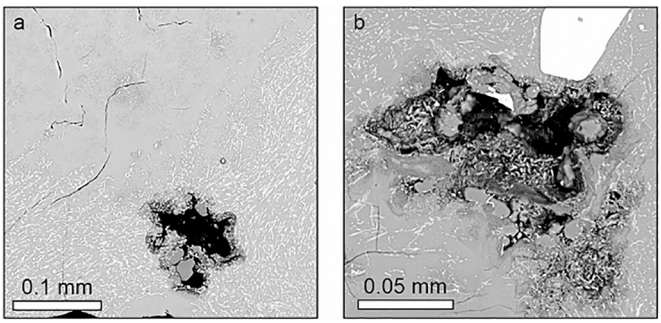

Fig. 7. SEM images showing cristobalite crystals internal to isolated pore spaces in the obsidian pyroclasts associated with diktytaxitic groundmass rims around the pore walls.

5.2. *In-vent lava surface red veneers*

We find that the red fracture surfaces (veneers) are frequently coated with sintered fine-grained particles (Fig. 8). In all cases (Fig. 8), the particles adhered to the lava surfaces in the red veneers have an average equivalent spherical radius of 0.25–3 μm and commonly feature necks (Fig. 8f) between the particles and adjacent or underlying particles. Farquharson et al. (2022) demonstrates that these particles are log-normally distributed in radius, with a mean centred on 1 μm and 2σ of 0.3 $\log_{10}$(μm), well into the 'very fine' volcanic ash fraction (grainsize on the 'phi scale' is $\varphi > 9$).

5.3. *Volcanic bombs*

The internal micro-texture of the bombs analysed here is variable. First, we note convolute, distributed, and locally angular pore networks (Fig. 9a) consistent with the general groundmass texture of moderately sintered samples (Quane and Russell, 2005; Heap et al., 2015; Gardner et al., 2019; Wadsworth et al., 2019, 2021b). In places, these same groundmass textures are less thoroughly sintered and occur in matrix veins, veinlets, or sutures (planar), often flanked by vesicular, pumiceous groundmass textures (e.g. Fig. 9b). Wisps of microlites are common features in the bombs, and are similar to the microlite wisps reported in the obsidian pyroclasts (Fig. 6). The wisps of microlites demarcate the margins between particles and the pore-space (Figs. 9c-d) and, in places where thoroughly sintered domains are immediately in the vicinity of slightly less-thoroughly sintered domains, it is clear that the microlite wisps are internal to the glass groundmass. In some sintered domains, there is evidence for shear deformation and particle alignment, especially in the veins and veinlets flanked by vesicular regions (Fig. 9e). In some of the bombs that contain incipiently sintered ash-dominated domains with sedimentary structures (Figs. 4j-l), the groundmass is clearly granular and sintered only sufficiently to confer coherency (Fig. 9f).

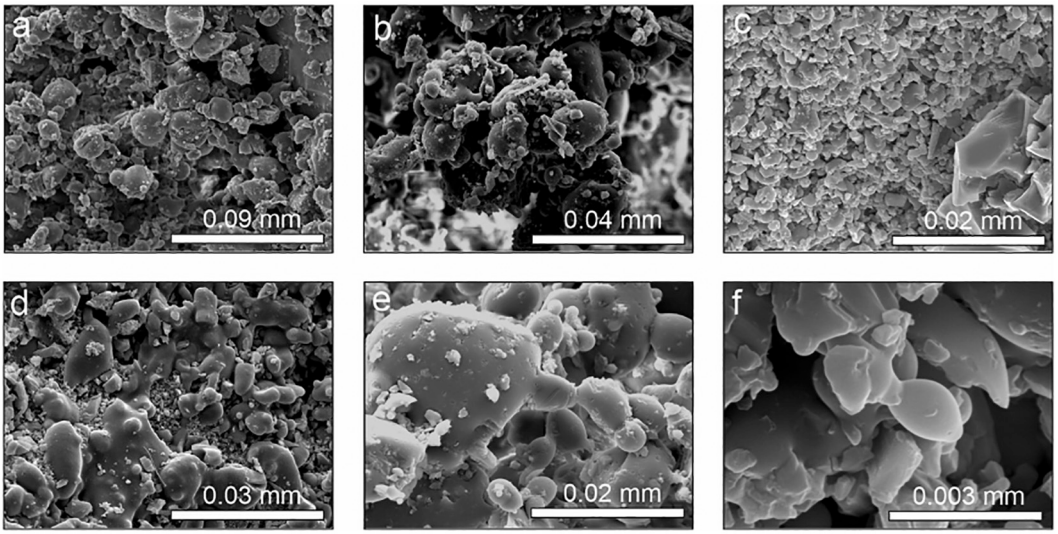

Fig. 8. Surface textures of the red-veneers on the in-vent lava fracture surfaces (see Fig. 2a-c). (a-c) Rounded and incipiently sintered fine ash particles adhered to one another in clusters. (d) Example of a region of more thoroughly sintered fluidal coatings. (e-f) Examples of clear neck formation between particles. (For interpretation of the references to colour in this figure legend, the reader is referred to the web version of this article.)

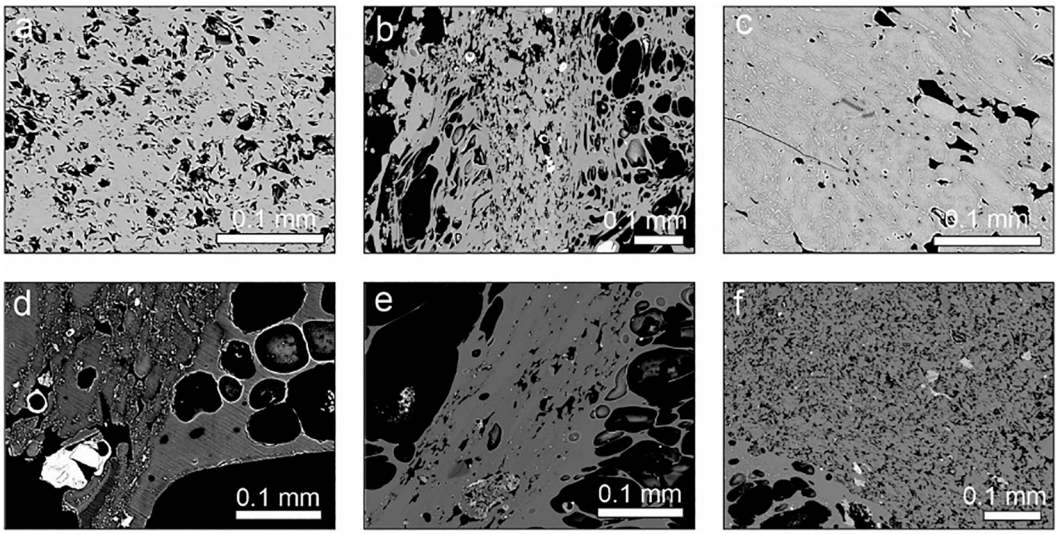

Fig. 9. Textures internal to volcanic bombs produced during hybrid activity (see Fig. 3). (a) Groundmass texture typical of moderately welded particles. (b) Central region of welded particles flanked by vesicular pumiceous regions (reproduced with permission from Schipper et al., 2021). (c-d) Welded particle boundaries are picked out by mineral coatings that appear bright under SEM. (e) Shear strain deformation of sub-rounded particles in a veinlet flanked by vesicular pumiceous regions. (f) Groundmass typical of poorly sintered, pseudo-granular particles.

6. Dissolved volatile concentrations

We find that the thermogravimetry data for the total volatile concentration – assumed here to be dominated by dissolved H_2O – in the samples of lava and lava veneers are consistently low when compared with the FTIR spot-analysis data for the total H_2O concentrations in the obsidian pyroclasts (Fig. 10). In Fig. 10 we additionally compile data from published sources for samples from Cordón Caulle 2011–2013, including: (1) total H_2O concentrations in 20–120 μm glass inclusions within plagioclase crystals found in fall deposit clasts from Castro et al. (2013); (2) calculations of total pre-eruptive H_2O concentrations from plagioclase hygrometry from Gilbert (2012); (3) total H_2O concentrations recorded in pumice and pumice lapilli from fall deposits from Castro et al. (2014); and (4) total H_2O concentrations recorded in volcanic bombs containing tuffisites, or composed of pumice breccia, also from Castro et al. (2014). We categorize these data according to the proposed eruptive style that produced them. First, pumice lapilli and pumice clasts are categorized as 'explosive'. Second, lava samples collected from the lava itself are categorized as 'apparently effusive'. Third, samples that contain evidence for tuffisites, or for brecciation-and-healing, or the obsidian pyroclasts, are all categorized as 'hybrid', based on the clear textural evidence for sinter-assembly presented previously (Castro et al., 2014; Schipper et al., 2021) and in Section 4b. We note that the lava itself was erupted during the hybrid phase, but is typically referred to as the 'effusive' component of that hybrid explosive–effusive behaviour.

By collating and categorizing the data in the way described, we find, in general, that the plagioclase hygrometry values and the glass inclusion values are clearly separated at high-H_2O relative to all other products, and are thought to be representative of the pre-eruptive H_2O concentrations; subject to uncertainties associated with the plagioclase enclosure time in the eruptive history and the potential for diffusive

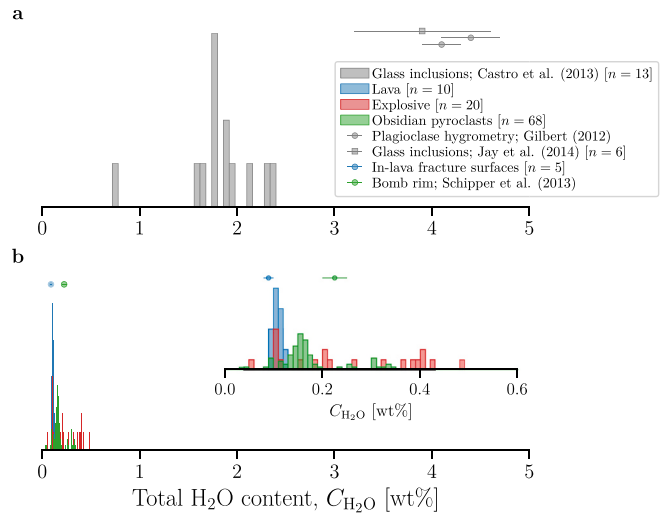

Fig. 10. Distribution of total H_2O concentrations (wt%) in eruptive products. (a) Glass inclusion analyses determined by Castro et al. (2013) and Jay et al. (2014) and plagioclase hygrometry calculations from Gilbert (2012). (b) Results of FTIR spot analyses on the lava, obsidian pyroclasts and pumice from the earliest phase of the eruption (pumice analyses from Castro et al. (2014)). Histogram bin size is 0.01 wt%. The TGA weight-loss analyses on the lava samples are given as a data point above the histogram labelled 'In-lava fracture surfaces'. *n* refers to the number of analyses in a given data population. Note that the y-axis in these distributions is omitted because the histograms are all normalized such that they are comparable, and the inset to (b) is a magnified plot of the same data presented in the main panel (b).

losses (Hervig et al., 1989; Wadsworth et al., 2020a). Similarly, the lava sample H_2O concentrations are clearly separated at the lowest overall values and mean value. However, we find that the H_2O concentrations for the explosive pumice products are similar to the distribution of H_2O concentrations found in the hybrid products, and that these two distributions (explosive and hybrid) overlap substantially.

As well as spot-analyses of dissolved H_2O concentrations in the obsidian pyroclasts, we additionally report constraints of the spatial distribution of dissolved H_2O concentration in three clasts (Fig. 11). These maps indicate broadly spatially homogeneous H_2O distributions. Given the low overall values represented in these spatial distributions, we posit that the clasts have equilibrated at shallow depths prior to quench (discussed later).

7. Lava fracture surface permeability

The permeability perpendicular to the fracture walls was measured to be $k = 2.64 \times 10^{-17}$ m^2 for lava samples for which the pyroclastic sintered veneer had been removed, representing the pre-sintering lava permeability. Samples with the sintered veneer had a permeability below detection at $k \ll 10^{-18}$ m^2, showing that the veneer reduced permeability by at least an order of magnitude, and thus restricted the efficiency with which gas could move laterally out of the fractures in response to gas overpressure.

8. Interpretation, analysis, and discussion: a reappraisal of hybrid behaviour

In this contribution, we have documented a range of textural and geochemical results for the products of hybrid explosive–effusive eruptions from the 2011–2012 eruption of Cordón Caulle. In order to frame our interpretations, we revisit principal observations of the explosive–effusive eruptive activity captured in January 2012 (Schipper et al., 2013), and from which we highlight two important features (Fig. 12). First, the in-vent lava clearly ruptures and supports fractures through which the gas and ash venting occurs, feeding the intermittent plume(s) (Figs. 12a-d). Second, the in-vent lava floor position rises and falls during venting. Together, these observations suggest that there is a source of pressurized ashy gas beneath the lava itself (Figs. 12d-f).

We interpret the textural record of the same hybrid eruptive behaviour as captured in the videography of the eruption (Fig. 12) in the context of the lava surface rupture and observed deformation. First, we note that any valid interpretation of the observations and measurements made herein should be consistent with the videography evidence, which shows that the intermittent, explosively generated, ash-rich plume, from which the fall deposits and uppermost tephra cone are constructed, is erupted *through* opening fractures in the lava itself. Similarly, a valid interpretation should be consistent with the time-resolved observations that show that the lava was advancing away from the vent area continuously during hybrid eruptive behaviour (Tuffen et al., 2013; Castro et al., 2014). The observation that the lava surface in the vent was apparently raised up in February 2012 relative to the flat-lying position observed in January 2012 (Fig. 12), is also consistent with a pressurized gas-dominated pocket beneath the lava pad. The nature of this gas pocket – as interstitial to a welding pyroclastic conduit 'rubble' – are discussed later (Section 8c).

Thus, near-vent observations of activity and macroscopic structures (ash-vents) in the emergent lava suggest that, despite the effusion of coherent lava, the shallow vent contained *incoherent* material, comprising a dynamic chamber containing broken magma with transient physicochemical behaviour. This conceptual model is summarized in Fig. 13. In the following section we discuss the connection between this sub-vent reservoir and the atmosphere.

8.1. Lava fractures as conduits for intermittent explosive behaviour

First, we propose that the red veneers on in-vent open lava fractures, which are themselves composed of sintered ultra-fine rounded ash particles, are the relict fractures through which gas and ash were explosively erupted, as seen in the videography (Fig. 3; Fig. 12). Indeed, the red veneers observed directly in the vent area itself (Fig. 1; Figs. 3a-c) are likely to be the last active lava fractures that were not rafted away from the vent area by continued lava advance. This interpretation implies that hybrid eruptive activity is required in order to generate these very-low-permeability veneer surfaces (Black et al., 2016). In turn, that implies that the cessation of hybrid activity occurred without further lava surface rafting from the vent area itself, because red veneers are preserved at the most proximal in-vent location (Fig. 3a). This is consistent with the suggestion that the continued lava medial and distal advance observed after hybrid activity had stopped (Tuffen et al., 2013) represented endogenous gravitational relaxation of a moderately overthickened flow (Farquharson et al., 2015; Magnall et al., 2017) rather than continued pressure-driven lava advance fed from the conduit. The similar fracture surfaces found in fractures in the distal lava (Figs. 3d-i), complete with tube filament structures that indicate sub-vertical orientation, are then interpretable as early lava fractures, which mediated some of the earliest hybrid explosive behaviour, that were subsequently rafted down-flow. This is consistent with the first observation of lava at the vent accompanying continued explosive activity, such that there was no clear break between exclusively explosive behaviour and the onset of hybrid behaviour defined by the presence of lava (Silva Parejas et al., 2012; Castro et al., 2013, 2014; Schipper et al., 2013). The lava fractures found in the distal lava show evidence for high shear strain of pseudo-tube pumice features on the walls of the fractures (e.g. Fig. 3g). We suggest that these could be interpreted in two ways. (1) These features could represent vesiculation of the fracture walls and that during vesiculation, the high mass eruption rate of a gas-ash dispersion through the adjacent open fracture exerts high shear stresses on the wall, resulting in large vesicle shear strains. And (2) high through-fracture flux of pumice clasts cause clast-wall bouncing and interactions, exerting sufficient shearing traction with the wall to both stick and deform

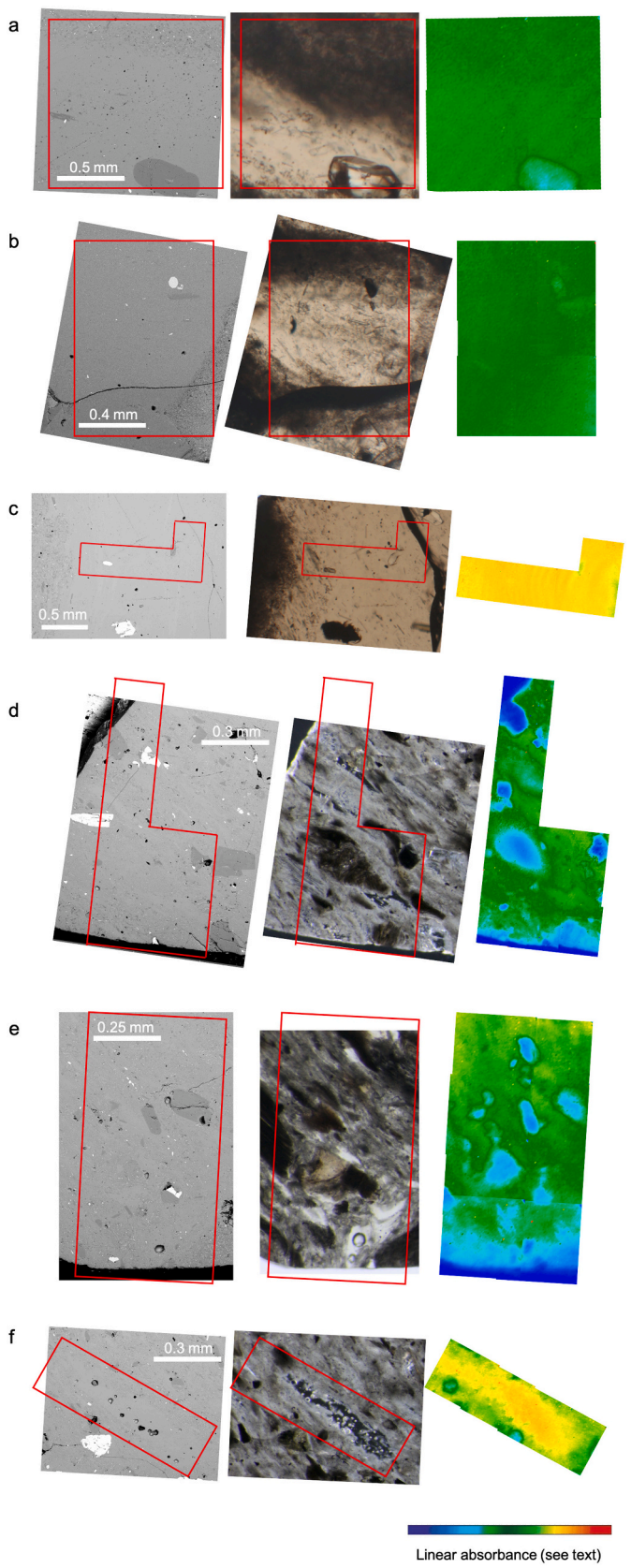

(caption on next column)

Fig. 11. The results of imaging FTIR analyses on obsidian pyroclasts. For each panel, there are 3 images which are (left to right), the SEM backscatter image, the reflected light image of the same region, and the spatial variation in 3500 cm^{-1} H_2O_t absorbance. For samples of uniform thickness, variation in H_2O_t absorbance corresponds to variation in H_2O_t concentration. Colour scale bar indicates linear variation in absorbance, which maps to a linear variation in concentration, with blue = 0.0 absorbance = 0.00 wt% H_2O_t. For CC1 (tiles a, b) red = 1.0 absorbance = 0.16 wt% H_2O_t; CC3 (tile c) red = 1.0 absorbance = 0.12 wt% H_2O_t; CC4 (tiles d, e, f) red = 0.8 absorbance = 0.51 wt% H_2O_t. The red box on the first two images refer to the position of the FTIR analysis in the third image. (For interpretation of the references to colour in this figure legend, the reader is referred to the web version of this article.)

against the wall as they are viscously captured. We propose that the latter explanation cannot be discounted, and is supported by the fact that similar tube-pumice textures are found in the purely explosive deposits (Schipper et al., 2013). It is possible, then, that deformed pumice – and even tube pumice – may here be formed by deformation of wall-bounded sintering clasts (c.f. Dingwell et al., 2016).

We interpret the oxidised pyroclastic fracture-fill remnant in the distal lava fractures (e.g. Figs. 3d-i) to be the variably welded trapped residue of the hybrid through-lava explosive phases: i.e. the pyroclasts that were left behind. Given that the hybrid plumes were intermittent, with waxing and waning explosive contributions to the eruptive behaviour (Schipper et al., 2013), it is likely that trapping of clasts was associated with the waning of explosive episodes. This is an interpretation broadly consistent with interpretations of tuffisite veins for which the host material either side of the pyroclastic fill is magma/lava (Saubin et al., 2016; Heap et al., 2019; Wadsworth et al., 2021b). Similarly, this explains the variable gradation between red-veneer material and orange-coloured coarse-grained pyroclastic fill (Fig. 3), where the gradation is broadly indicative of waning mass flux through the fractures. These fractures do not contain much evidence for bulk deformation, suggesting that they have been rafted on the lava top during lava advance intact, similar to the observation of segments of the tephra cone that have been rafted away from the vent area broadly intact (Fig. 1).

Pyroclastic features found within silicic lava fractures have been described previously (Iddings, 1888, 1899; Boyd, 1961; Sparks et al., 1993; Manley, 1995, 1996; Black et al., 2016). Both Manley (1995) and Manley (1996) suggest that these are the product of in-situ and flow-related rupture at buckling lava crusts. Rupture of flowing lava is clearly possible, evidenced by the rubbly tops and flow fronts (Fig. 1), and by large fractures found elsewhere, produced in viscoelastic lava itself (Wadsworth et al., 2018; Andrews et al., 2021); however, the production of fine and ultra-fine ash (Figs. 3 and 8, respectively), all sintered to these fractures, is hard to reconcile with post-eruptive lava emplacement mechanisms. Instead, our model provides a direct link between the primary fragmentation at depth and the material found in these fractures, which may be subsequently rafted down-flow.

8.2. Obsidian pyroclasts as markers of shallow in-conduit sintering and eruption cycles

Obsidian pyroclasts were found in abundance in the tephra cone around the vent, and represent part of the tephra load that was explosively released through the conduit and fractures during hybrid activity. The obsidian pyroclasts show textural evidence for planar fractures with adhered material (Figs. 5a-b), sintered groundmass pore textures (Figs. 5d-f; c.f. Rust et al., 2004; Gardner et al., 2017, 2019), the incorporation of pumiceous ash particles (e.g. Figs. 5g-i), and incomplete sintering in pore spaces preserving cuspate interfaces (e.g. Figs. 5j-l). In all cases, we interpret the obsidian pyroclasts as the product of in-conduit sintering, consistent with recent work (Gardner et al., 2017, 2019; Wadsworth et al., 2020a; Monnereau et al., 2021; Wang et al., 2021). In particular, the domains of high relative microlite content and sintering-like pore structures in domains within a groundmass of glass

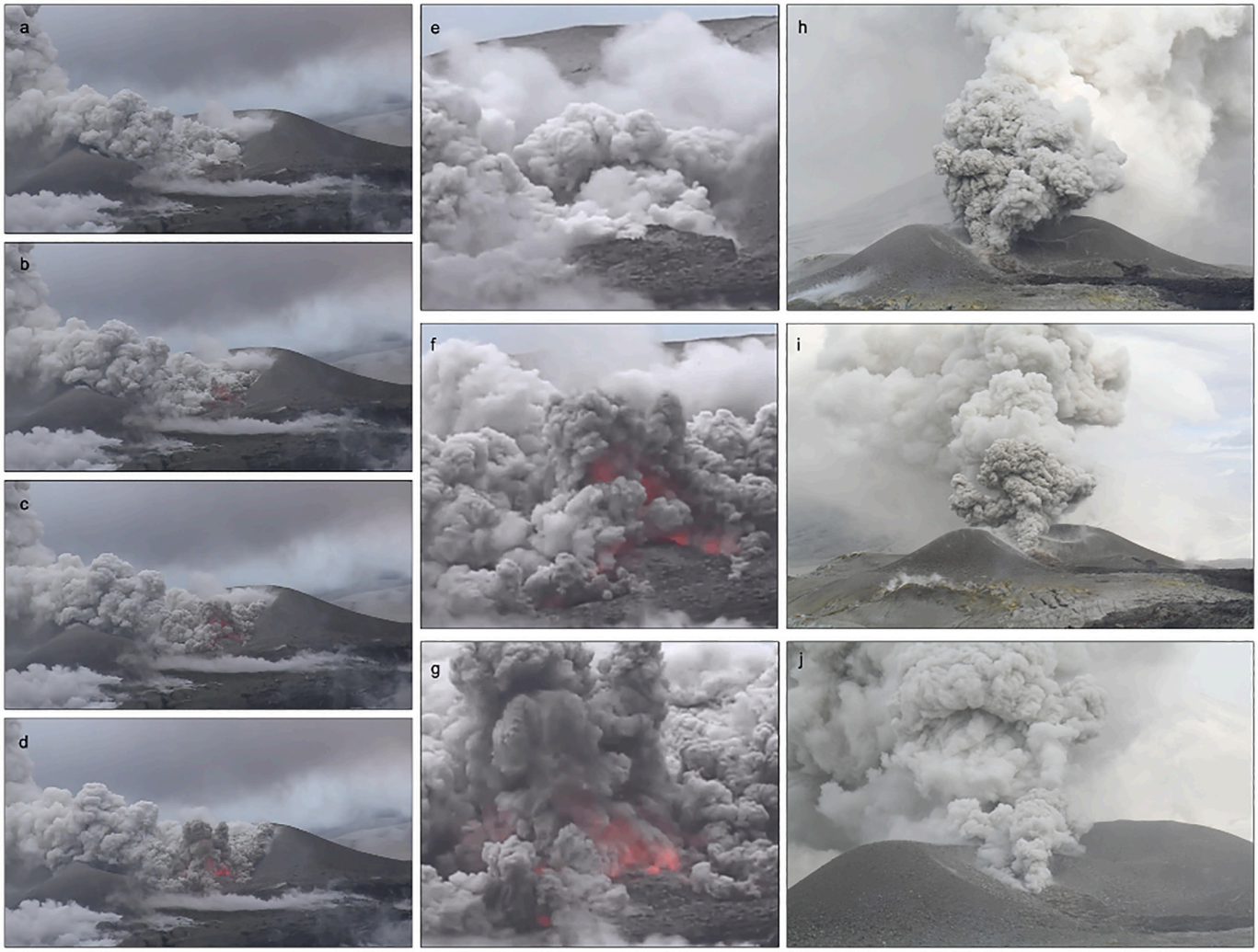

Fig. 12. (a-g) Still images from a video of the hybrid phase of the eruption collected in January 2012 (c.f. Schipper et al., 2013). (a-d) Four different times separated by 3 s intervals. (e-g) Cropped zoom-in of the evolution of a pad of the lava (visible in the foreground of (e) surrounded by gas and ash jets) as it (f) opens up, lifts, hosts incandescent gas-ash jetting, and then (g) falls down again. Panels (e-g) are separated by 3 s intervals. (h-j) Photographs of the eruption taken in February 2012 (contemporaneous with the image in Fig. 2). Note that the lava seen in (j) is 'perched' relative to the lava pad surface in (a-d), and after the eruption (Fig. 1d).

(e.g. Fig. 5d) suggest more than one sintering episode may have occurred. The juxtaposition of domains of very high and very low groundmass crystallinity are hard to explain without those co-located domains originating from very different pressure histories. The vesicular ash particles captured in the obsidian pyroclasts (Fig. 5g) and the remnant sub-rounded cuspate particles trapped in pore spaces (Fig. 5j) allow us to estimate a ~30 μm particle radius for the sintering, acknowledging that we cannot place a lower bound on this size given that original pyroclast sizes have been obscured during the sintering process. Importantly, whereas obsidian pyroclasts have previously been investigated within the products of widespread Plinian or sub-Plinian fall deposits (Rust et al., 2004; Gardner et al., 2017), the pyroclasts investigated herein preserve similar sintering histories well into hybrid explosive–effusive behaviour (Fig. 5).

The uniformly low H_2O concentrations preserved in the obsidian pyroclasts from the upper tephra cone at Cordón Caulle are striking, given that obsidian pyroclasts from many silicic volcanoes preserve variable, and much higher, residual H_2O contents (Watkins et al., 2017). This suggests that the obsidian pyroclasts produced during hybrid activity are the products of sintering at very low H_2O vapour pressures, consistent with the shallowest depths in the conduit. This is in turn supportive of the shallow conduit being occupied, at least transiently, by a gas and ash-rich pocket in which the obsidian pyroclasts may form through sintering. It is not possible to interpret the H_2O concentrations quantitatively in terms of depth in the conduit, because our interpretation of the mechanism of their formation implies that they were formed above the primary magma fragmentation depth by sintering to in-conduit fracture walls, before being plucked off, and erupted as sintered pyroclasts. This implies that the conduit was wholly open-system with a complex dependence of gas pressure on depth that could vary substantially (c.f. pressure distributions supra-fragmentation in conduit models; Degruyter et al., 2012) as mass eruption rates waxed and waned (Schipper et al., 2013). However, the lower bound on the dissolved H_2O concentration measured in the obsidian pyroclasts is 0.09 wt.% H_2O, which is consistent with a partial pressure of H_2O of <1 atm at any eruptive temperature up to 1000 ° *C*, suggesting that the sintering likely occurred in a mixed gas environment (atmospheric and magmatic contributions) at very shallow depth. This will be discussed further in Section 8d.

In contrast to the uniformly low H_2O concentrations measured in the obsidian pyroclasts, we see a slightly greater spread of H_2O concentrations in the obsidian pyroclast chunks that are embedded within the ash-rich bombs (Fig. 4l). These H_2O contents span a range extending from the driest of obsidian pyroclasts (~0.10) to about a half a weight percent H_2O. Interestingly these variably hydrous clasts occur within centimetres of one another within the bomb and are encased in the same ashy

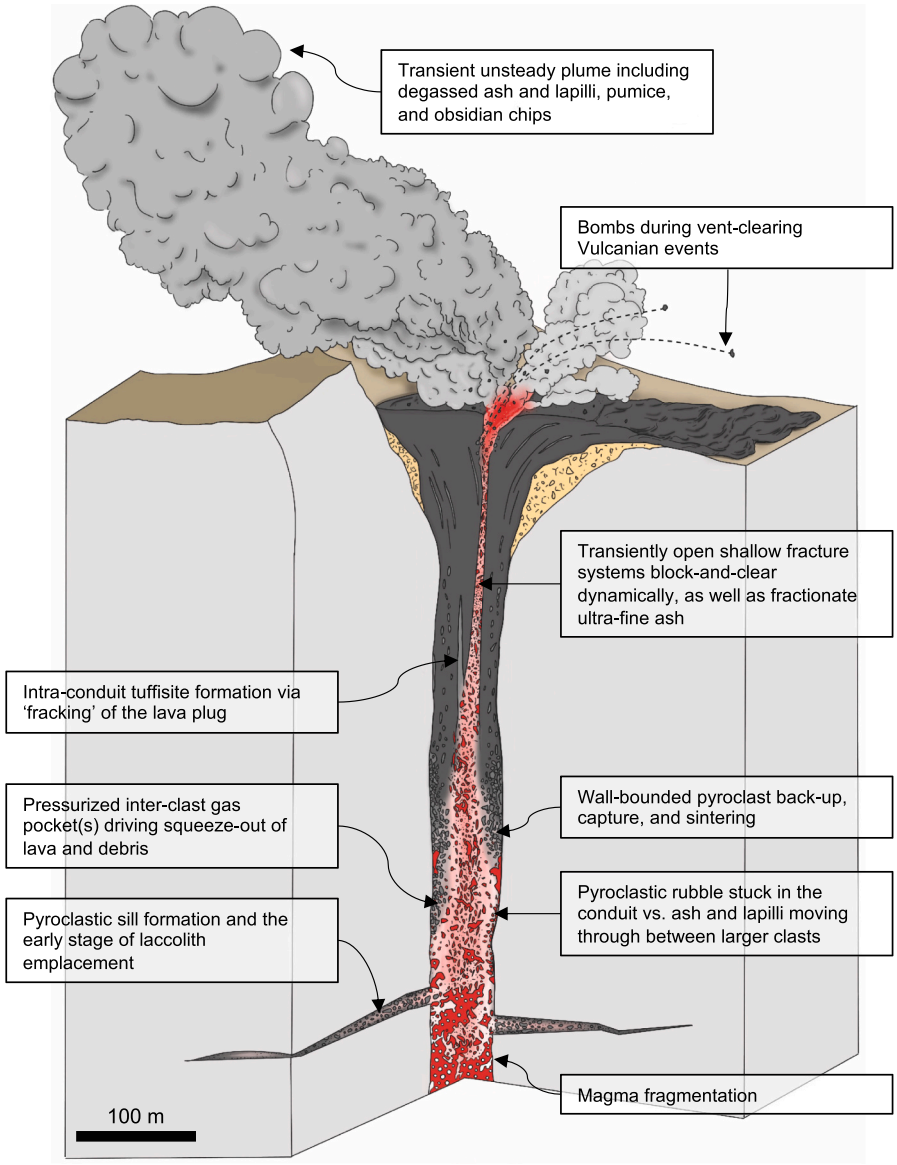

Fig. 13. Conceptual picture of the immediate subsurface magma system fuelling hybrid activity at the 2011–2012 eruption of Cordón Caulle. The details depicted here draw on the direct results of this study, as well as some conceptual synthesis from observations presented in other work on the same eruption. Our model is underpinned by the model of Wadsworth et al. (2020a) who suggest that the shallow lava can be assembled from the products of sustained or intermittent primary magmatic fragmentation, divorcing apparently effusive products from the classical interpretation that they represent the buoyant rise of magma from storage regions to the surface. In this new paradigm, pyroclastic sill emplacement is likely above fragmentation (Unwin et al., 2021) consistent with the onset of shallow laccolith emplacement (Castro et al., 2016; Zheng et al., 2020). The gas–pyroclast rubble underlying the erupting lava provides the pressurized ash-laden sustained gas source required to explain rapid effusion rate and associated pseudo-harmonic tremor (Bertin et al., 2015), lava- and country-rock hosted tuffisites (Castro et al., 2012, 2014; Heap et al., 2019), intermittent fracture-fed plumes and bombs (Schipper et al., 2013), and pervasive sintering textures in all primary products of the hybrid phase (Schipper et al., 2021).

and partially sintered matrix, suggesting a high energy provenance (a turbulent, fluidised, ash-and-gas pocket within the conduit).

Cristobalite preserved in isolated pore spaces in some obsidian pyroclasts (Fig. 7) can be interpreted to represent the local redistribution of silica in the presence of acidic fluids (Damby, 2012; Schipper et al., 2015, 2020; Kushnir et al., 2016; Martel et al., 2021). At Cordón Caulle, this has been observed in samples of the lava itself, and inferred to represent variable temperature dissolution of the groundmass glass during relatively slow cooling, and the eventual deposition of silica from the saturating fluid phase in the isolated vesicle (Schipper et al., 2015, 2020). Therefore, in the context of the obsidian pyroclasts, we can extend this interpretation to suggest that this implies a stagnation time during and immediately following sintering of the pyroclast in-conduit, sufficient for the dissolution of groundmass to occur, before eruption and quenching of the bulk pyroclast. Complete sintering involves the total isolation of pore space (Wadsworth et al., 2016a, 2019), setting the conditions for the closed-system redistribution of silica inferred. Similarly, the eruptive quenching of the pyroclast would involve a drop in silica solubility in the fluid phase (Manning, 1994), and could promote the precipitation of the cristobalite on vesicle walls, or vesicle-penetrating plagioclase crystals (Schipper et al., 2020).

We interpret the wisps of microlites observed in the obsidian pyroclasts (Fig. 6) as syn- or post-sintering devitrification textures, possibly associated with high-temperature gas-ash reactions (Delmelle et al., 2018; Wadsworth et al., 2021a). The textural evidence that these crystals invade the groundmass either side of the interface or former interface prior to sintering suggests that they are not purely precipitated on the surfaces from the vapour phase, and do indeed involve growth from the melt itself. Nevertheless, this suggests that, in pyroclasts for which there is no direct evidence for a pre-sintering pore phase, these microlite wisps trace former ash-gas interfaces that have been sinter-sealed at high temperature. This is in turn consistent with the less thoroughly sintered examples in the volcanic bombs (see Figs. 9c-d) in which the same wisps can be seen at the margins of incipiently sintered particles.

Obsidian pyroclasts have been described previously (Rust et al., 2004; Gonnermann and Manga, 2005b; Rust and Cashman, 2007; Gardner et al., 2017, 2019; Watkins et al., 2017; Monnereau et al., 2021; Wang et al., 2021). Theories for their formation generally fall into two categories: (1) shear rupture and brecciation at the margins of ascending magma *below* any wholesale fragmentation depth (Rust et al., 2004; Gonnermann and Manga, 2005b), or (2) sintering at the margins of conduits *above* the fragmentation depth and in the free gas phase of an

open-conduit (Gardner et al., 2017, 2019; Wadsworth et al., 2020a). While none of the textures presented here (Fig. 5) necessarily preclude model (1), in the context of the wider findings of this work, in which there is evidence for wholesale fragmentation and re-sintering, we favour model (2). We additionally suggest that obsidian pyroclasts produced well into a hybrid explosive–effusive eruptive phase may be produced shallower and at lower partial pressures of H_2O than those produced earlier in an eruptive cycle within the explosive phase (Watkins et al., 2017), possibly unifying the diverse range of H_2O–CO_2 compositions of obsidian pyroclasts reported to date.

8.3. Volcanic bombs as indicators of the broader sub-surface and sub-lava conduit fill

The interpretation provided in Sections 5a and 5b is broadly consistent with a model in which the shallow lava is assembled by progressive sintering and concomitant extrusion of the sintered product (Wadsworth et al., 2020a). This coherent lava is intermittently fracked, producing open, through-lava fractures and tuffisite-valve dynamics (Castro et al., 2012, 2014). However, the volcanic bombs produced during hybrid activity at Cordón Caulle are more complex in terms of their componentry (Schipper et al., 2021). They preserve similar evidence for general sinter-assembly (Figs. 4 & 9), but are clearly composed of not only ash particles, but also pumice, obsidian pyroclasts, and lithics in varying proportions (Fig. 4; Schipper et al., 2021). The components of the bombs are not dissimilar to those found in the distal rafted open lava-fractures (Fig. 3), albeit more variable and mostly less oxidised. Whereas the bombs are rich in fine ash (e.g. Fig. 4), some of the distal fracture surfaces are mostly fines-poor. Here, we interpret the composite bombs as indicative of the bulk of the volcanic subsurface between the fragmentation depth and the shallower depth at which the lava is being assembled on the conduit walls. In this region, Wadsworth et al. (2020a) speculated that there could be a clast-supported rubble of pyroclasts, which would densify by a combination of sintering and internal collapse of larger pumiceous clasts. This broad scale picture of a sub-volcanic conduit-filling rubble (Adams et al., 2006) is consistent with the textures reported in Figs. 4j-l. The highly heterogeneous sub-clast componentry of these bombs is held together by variably sintered fine ash, implying that the component clasts were assembled in an environment in which they were bathed in, intruded by, or fractured by, continuous dilute flow of sintering and depositing ash particles that sutured the components of the bombs into coherent masses. A conduit filling pyroclastic rubble of pumice bombs, lapilli, and lithics, would be mixed in a granular manner, as well as being continuously or episodically shot-through with fines that would variably adhere to, or permeate through, larger clasts. Similarly, gas pressures interstitial to such a rubble would fluctuate as continued deeper fragmentation added mass to the gas phase, and shallower lava production variably occluded or even sealed the vent (c.f. Fig. 12). We conclude that all textures in Figs. 4 & 9 are consistent with this interpretation, and cannot readily be explained without a sub-surface clastic fill to the vent.

The observation that some ash-bearing volcanic bombs contain obsidian pyroclasts welded into their granular matrix (Figs. 4j & 4l) demonstrates that obsidian pyroclasts and bombs are produced in the same region of the sub-volcanic system, or at least in regions between which material is readily transferred. Similarly, these two features can be formed over similar timescales (Schipper et al., 2021), consistent with the observation that they can be juxtaposed and assembled together. The 2011–2012 eruption was likely dyke-fed (Castro et al., 2013), as was the similar 1960 eruption at this same volcano (Lara et al., 2004). We propose that along-strike variations in the dyke-like conduit could be substantial (Schipper et al., 2021) and that the nature and transport of material in the conduit was heterogeneous, and subject to transient spatial organisation, as evidenced directly in the eroded and exposed sub-volcanic plumbing at Hrafntinnuhryggur in Iceland (Tuffen and Castro, 2009). In this broad framework (Sections 5a-c), the eruption of volcanic bombs is likely to represent pulses of elevated gas pressure in the open and permeable sub-volcanic, supra-fragmentation region, excavating some of the conduit-filling rubble and lithics (seen in the fall deposits in the upper tephra cone; Fig. 1). At episodes of lower relative eruptive energy, bombs would not be erupted and instead gas and ash would percolate rapidly between the rubble clasts and produce ash venting through the assembling lava. This conceptual model can explain the direct observations made during the eruption (Fig. 12; Schipper et al., 2013).

8.4. Conduits as large-scale tuffisites: percolative ash-laden flow through conduit-filling rubble

Clast-filled volcanic fractures – preserved as tuffisites – in conduits with variable evidence for dilute transport mechanisms, tractional bedforms, variable sintering, and internal structure, are reported at a range of volcanic settings (Stasiuk et al., 1996; Tuffen et al., 2003; Tuffen and Dingwell, 2005; Castro et al., 2012; Cabrera et al., 2015; Black et al., 2016; Saubin et al., 2016; Farquharson et al., 2017; Casas et al., 2019; Heap et al., 2019). Typically, these are interpreted as the product of shear-fracturing of coherent magma, with no specific explanation of how the particulate fill is formed at such fine grainsizes, nor how it is fluidized or how the production and emplacement of the dilute particle dispersion is sustained (Tuffen and Dingwell, 2005). If, instead, the formation of these fractures is tensile and they form by gas overpressure-driven fracture formation in the host lava, accompanied by rapid ingress and through-put of pyroclastic material produced beneath, then the fracture-bounded flow of particles can be sustained and replenished continuously (Wadsworth et al., 2020a; Unwin et al., 2021; Farquharson et al., 2022). Where these are found in a lava host rock, this is consistent with our broad interpretation of the pyroclastic fracture fill found here in the lava (Fig. 3). Previous work has either disregarded the source of the pyroclasts, or inferred them to be from the disaggregation of (1) local fracture wall rock (Tuffen and Dingwell, 2005), (2) a foamy region of coherent magma underlying the dense lava plug (Saubin et al., 2016), or (3) a 'deep' but un-constrained source (Berlo et al., 2013). The production of ultra-fine ash typically requires a very high pressure drop at fragmentation (Alidibirov and Dingwell, 1996; Kueppers et al., 2006; Fowler and Scheu, 2016) or granular disruption above fragmentation (Dufek et al., 2012). Given the many lines of evidence for the clastogenic nature of the lava deposits (Wadsworth et al., 2020a), we consider it more likely that the fracture fills both in tuffisites and in the in-lava fractures reported here, are sourced from primary fragmentation at depth. This is, in turn, consistent with the nature of the volcanic bombs, which record clear pyroclastic origins, and which are common among all the bombs erupted – suggesting that a large portion of the volcanic subsurface is built of sintering clasts and not of coherent foamy magma. We note that our model *does* require that coherent foamy magma exists below and up to the fragmentation front, as envisaged in standard models of explosive eruption.

The dilute ash deposits within bombs (Fig. 4) have previously been interpreted to be tuffisites (Paisley et al., 2019a), however, the evidence that the sub-volcanic region may host a large region of pyroclastic rubble (Wadsworth et al., 2020a; Schipper et al., 2021) opens up the possibility that what appear to be veins of ash deposits in fractures are actually deposits from continuous percolative flow through the inter-clast interstices of the rubble, essentially blocking up some of the rubble pathways. This model requires a rubble-filled sub-volcanic conduit, and explains the observation of altered and wall-rock lithics in the welded material (Saubin et al., 2016; Heap et al., 2019). In the following sections (8e-g) we test the feasibility of this model through examination of particle size distributions, and timescales of transport, degassing, and sintering of clastic material in the conduit.

8.5. Grainsize fractionation, permeability evolution, and plugging the upper conduit

We compile the grainsize distributions published for each of the component granular products of this eruption (Fig. 14): (1) the lava fracture surfaces (Fig. 8; Farquharson et al., 2022); (2) the particles observed internal to the bombs (Fig. 9; Schipper et al., 2021); and (3) the reconstructed total grainsize distributions for the fall deposits from the dominant explosive phase(s) (Costa et al., 2016; Reckziegel et al., 2019). Note that these reconstructions account for down-plume sorting and aim to represent the total grain size distribution erupted at the source vent. The mean grainsize (radius) for the in-lava fracture veneers is 4.56×10^{-7} m, and for the particles found in the bombs it is 7.41×10^{-6} m.

It is clear that the total grainsize distributions for the fall deposits found at the Earth's surface are coarser than the fines captured by in-vent processes (Fig. 14), which are wholly absent from the Reckziegel et al. (2019) reconstruction. Wadsworth et al. (2020a) suggest that, if lava is produced by in-conduit sintering, then it is likely that there would be a grainsize fractionation effect, such that the finest particles produced at magmatic fragmentation would be those preferentially captured and welded in the conduit, and would therefore be under-represented in the plume. This is further explored by Farquharson et al. (2022), who suggest that this is principally because the capture and sintering dynamics are dependent on grainsize, such that ultra-fine ash (Fig. 8) and ash (Fig. 9) can be captured more easily than coarser particles such as lapilli. This is consistent with the fine-grained nature of the in-conduit deposits or deposits inferred to have been captured and then erupted (Fig. 14). This implies that the uppermost conduit may act as a pyroclast filter, removing the finest fraction from the plume and ultimately from the deposits. Recognition of pumice aggregates in silicic pyroclasts (Giachetti et al., 2021) further reinforces the decoupling between grainsize distributions generated in subsurface fragmentation and emitted at the surface. Giachetti et al. (2021) interpret the pumice aggregates they describe to have formed without stalling and capture in the conduit; we suggest that they could equally have been formed by sintering at the conduit walls or during stalling in-conduit in a pumice rubble. Indeed,

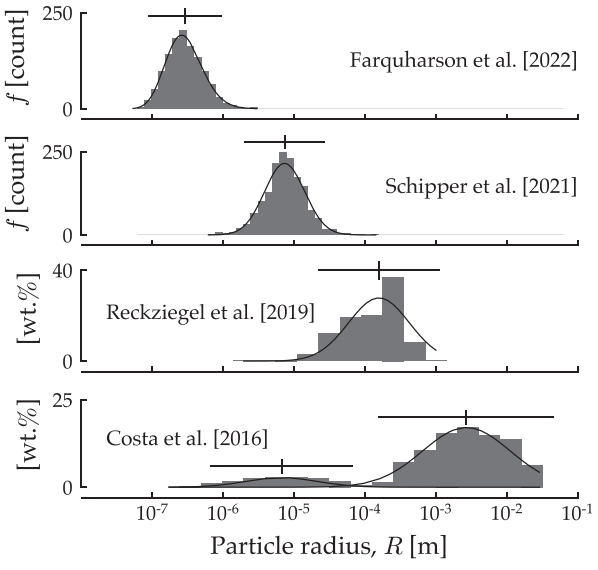

Fig. 14. Particle size distributions associated with the 2011–2012 Cordón Caulle eruption. (a) Data from Farquharson et al. (2022) for the in-lava fracture surfaces (see Fig. 5). (b) Data from Schipper et al. (2021) for the particles partially welded in volcanic bombs. (c-d) Total grain size distribution reconstructions (by two different methods) for this eruption based on fall deposits (Costa et al., 2016; Reckziegel et al., 2019). In panels (a) and (b) we fit log-normal distributions to the data and display the mean of the fitted distribution with a range given by the standard deviation on the mean.

the turbulent nature of the primary fragmentation event involves vigorous clast accelerations that are likely to preclude long contact times between pumice clasts in primary transport proximal to the fragmentation front. Particle stalling between fragmentation and the surface, as envisaged in our model, provides the time at low collision frequencies required for sintering to produce aggregates.

8.6. Degassing pyroclasts: reconciling the ubiquitously low H_2O concentrations in the hybrid eruptive products

The H_2O concentrations in the hybrid eruptive products are ubiquitously low, and seemingly similar regardless of the ultimate deposit measured (e.g. obsidian pyroclasts, pumice, lava veneers, or bombs; Figs. 10 & 11). In the framework of our interpretation for hybrid explosive–effusive behaviour, the lower-bound on the time available for diffusive pyroclast degassing above fragmentation λ is broadly given by the average transport time $\lambda = L/u$, where L is the depth to fragmentation, and u is the average velocity of the pyroclast through the fractures in the lava or up through the pyroclastic rubble beneath the assembling lava. Direct observations yield an approximate value of $u = 50$ ms^{-1} (Schipper et al., 2013), which we assume is broadly constant from fragmentation to the surface. In order to explore a reasonable range for λ, we take an upper bound and a lower bound on L of $2000 \leq L \leq 500$ m from previous conduit models and conduit model applications (Mastin, 2002; Degruyter et al., 2012; Cassidy et al., 2018; Wadsworth et al., 2020a).

A pyroclast will be thoroughly degassed if $\lambda > \lambda_d$, or equivalently, if the normalized time $\bar{t}$ exceeds unity, given by $\bar{t} = \lambda/\lambda_d > 1$, where $\lambda_d = R^2/D$ is the time required for diffusive degassing; here R is the pyroclast radius and D is the diffusivity of H_2O. Using a constitutive diffusivity model for rhyolites (Zhang and Ni, 2010), we account for the dependence of D on temperature, pressure, and the local concentration of H_2O. Considering a temperature of 900 ° C and a wide range of pressure between 0.1 and 2 MPa (upper conduit values above fragmentation; Unwin et al. (2021)), and using this to compute the equilibrium solubility of H_2O (using Liu et al., 2005), as a guide for the H_2O concentration at a given pressure, we find that D varies by up to an order of magnitude ($6.8 \times 10^{-12} \leq D \leq 3.4 \times 10^{-13}$ m^{2}s^{-1}). We use this range to provide a range of λ_d for a given R.

By the analysis described here, $\bar{t}$ varies inversely with R^2; hence, over the wide range of particle size of interest here of $10^{-7} \leq R \leq 10^{-1}$ m (see Fig. 14), R dominates over the range of D and L that we consider, such that $\bar{t}$ for a given R is similar compared with the range in $\bar{t}$ over all R considered, regardless of these choices. The transition from thoroughly degassed $\bar{t} > 1$ to poorly degassed $\bar{t} < 1$ therefore occurs over a small uncertainty in R, where the critical radius for this transition is $R_c = \sqrt{LD/u}$ and is $5 \times 10^{-6} \leq R_c \leq 1 \times 10^{-5}$ m. This is consistent with the estimate for the critical radius for in-conduit degassing during transport found using a full numerical approach ($R_c \sim 10^{-5}$ m; Wadsworth et al., 2020a). In Fig. 15 we give the solution to this simple scaling approach for $\bar{t}(R)$ along with the distributions from Fig. 14, showing that the particles associated with the in-lava veneers are consistent with $\bar{t} > 1$, while the in-bomb sintered particles are consistent with $\bar{t} \sim 1$, and the plume-derived total grain size distributions are almost all consistent with $\bar{t} < 1$.

The scaling analysis presented here shows that ultra-fine ash has $R < R_c$, such that $\bar{t} > 1$, explaining why the ultra-fine ash in the lava veneers are fully degassed. We take 'fully degassed' to mean a measured H_2O concentration of $\lesssim$0.1 wt%, which is the equilibrium value for degassing to atmospheric partial pressure of H_2O (von Aulock et al., 2017; Wadsworth et al., 2019; using Liu et al., 2005). By contrast, the majority of the pyroclasts in the total grain size reconstructions (Costa et al., 2016; Reckziegel et al., 2019) have $R > R_c$ such that $\bar{t} < 1$; hence, much of the widespread fall deposits is expected to be less than fully degassed in the atmosphere, and host some elevated H_2O concentrations, which is

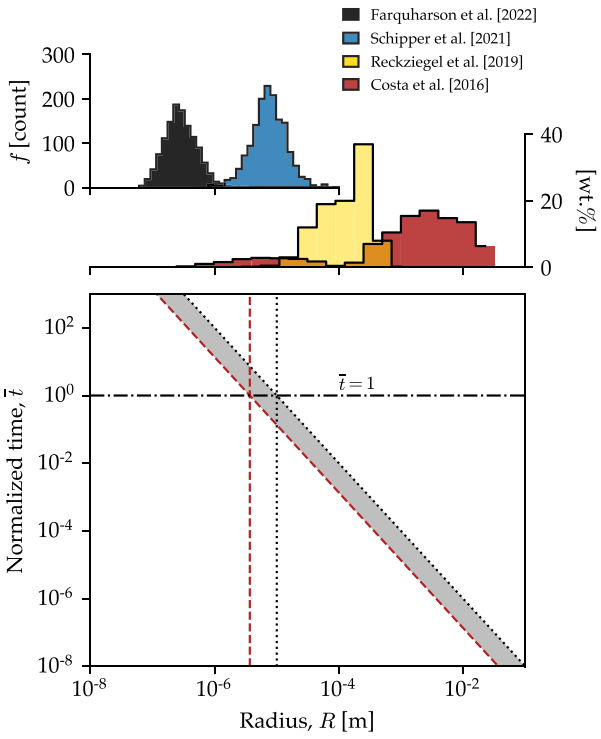

Fig. 15. Scaling for the normalized time $\bar{t}$ required for degassing in particles of radius R, where $\bar{t} \sim tD/R^2$, where t is the travel time of particle given by the ratio of the depth to fragmentation L to the particle velocity u. The upper bound (dotted black curve) is given by $D = 2.52 \times 10^{-12}$ m^{2}s^{-1}, $L = 2000$ m, and $u = 50$ ms^{-1}, and the lower bound is given by $D = 3.41 \times 10^{-13}$ m^{2}s^{-1}, $L = 500$ m, and $u = 50$ ms^{-1} (see text for details). These relate to critical radii for which $\bar{t} = 1$ of $R_c = 1.06 \times 10^{-5}$ m and $R_c = 5.02 \times 10^{-6}$ m, respectively, consistent with full numerical solutions based on conduit flow models (Wadsworth et al., 2020a).

consistent with some of the H_2O analyses for the explosive products (Fig. 10). Finally, it is clear that the bombs and obsidian pyroclast size distributions straddle R_c so that $\bar{t} \sim 1$. This is consistent with the wide variability in both the H_2O concentrations measured (Fig. 10), and in the spatial distributions of H_2O concentration (Fig. 11), with some domains internal to the obsidian pyroclasts recording elevated H_2O concentrations (Fig. 11f). However, it is also clear from the raw data (Fig. 10) that these differences are small compared with obsidian pyroclasts from other rhyolitic fall deposits, which may exhibit more than ~2 wt% variation in bulk H_2O content (Rust et al., 2004; Gardner et al., 2017; Watkins et al., 2017). In those studies, pyroclasts were collected from medial to distal fall deposits and thus represent activity early in the eruptive sequence rather than from shallow conduit-mediated hybrid eruption behaviour (Rust et al., 2004; Gardner et al., 2017; Watkins et al., 2017). Therefore, while obsidian pyroclasts may be formed from the earliest parts of explosive behaviour (Gardner et al., 2017), they may become more thoroughly degassed as an eruption shifts to hybrid behaviour and the formation window of the pyroclasts by sintering shallows.

8.7. Permeability

The grainsize of the pyroclasts (Sections 8e & 8f) involved in the conduit sintering processes directly impacts the permeability evolution as sintering occurs, which is crucial for understanding the 'openness' of the upper conduit at a given moment in time, hence the outgassing behaviour from the upper conduit and the propensity for gas pressure build up. We compile permeability data for deposits from Cordón Caulle (Heap et al., 2019; Schipper et al., 2021) and from experimental sintering of rhyolite ash-size particles (Wadsworth et al., 2021b), and find that all data are consistent with a grainsize-dependent model for the covariance of permeability with porosity (Wadsworth et al., 2016b, 2021b) for a mean radius of 6.24×10^{-6} m (Fig. 16). This is highly consistent with the grainsize found in the bombs and lava surfaces (Fig. 14).

In addition, our laboratory measurements show that the veneers on lava fracture surfaces substantially lower the permeability in the lateral outgassing direction (Section 4d). Similarly, Schipper et al. (2021) showed the sintered, clast-supporting matrix in the composite bombs substantially lowered permeability of the sub-volcanic rubble that had been sutured together relative to an unsintered fragmental mass. Taken together, these observations and model results suggest that the sintering substantially lowers the permeability of the upper conduit, whereas clearly the intermittent explosive behaviour that clears the fractures, erupts bombs, and opens up fractures in the lava pads acts to re-open the system. Therefore, the grainsize fractionation effect is likely to be accompanied by transient opening and closing of the upper conduit, consistent with the direct observations of the hybrid behaviour (Fig. 12).

9. Implications

In Section 8, we have presented our interpretation of the results of this study. Our central model for in-conduit processes during hybrid effusive–explosive activity is summarized in Fig. 13. This conceptual model synthesizes our own observations, data, and analyses, with those from the published literature. The model differs most notably from previous models in two regards: 1) apparently effusive lava is assembled via the shallow sintering of the products of deeper, cryptic fragmentation; and 2) the shallow conduit is filled with a rubbly mixture of primary pyroclastic material, variably sintered and welded clasts, and gas, rather than with coherent magma. In this section, we explore further implications of our interpretations for silicic eruption dynamics in general.

9.1. Obsidian: sintering to form low-crystallinity dense lava and similarities with ignimbrites

During explosive eruptions, pyroclasts that are deposited from pyroclastic density currents at high temperatures (close to magmatic temperatures) can weld to form glassy, obsidian-like deposits, termed vitrophyres, in ignimbrites (Andrews and Branney, 2011; Lavallee et al., 2015; Monnereau et al., 2021). These are low-porosity or wholly non-porous deposits of aphyric volcanic glass, with variable – and often scant – evidence for their own welding origin. It is precisely because the welding process leading to such vitrophyre deposits often overprints most of the evidence for their own genesis, that they can be misinterpreted as lavas (Branney and Kokelaar, 1992; Manley, 1995). It is for this reason they are usually called 'lava-like' ignimbrites (Branney et al., 1992; Branney and Kokelaar, 1992, 2002). In such cases, there are other, sometimes indirect, pieces of evidence that are used to confirm that the now coherent and dense deposit was formed from the amalgamation of pyroclasts and ash (such as a non-brecciated ignimbrite base). Our model presented here extends these ideas into the volcanic sub-surface, and suggests that obsidian domes and lavas may be assembled by this same hot pyroclastic deposition, ultimately obscuring much of the primary evidence that it occurred (Wolff, 1986). The key difference in our model is that this welding/sintering occurs in-conduit and not on the Earth's surface. Just as vitrophyres overprint much of the internal direct evidence that they originate from sintering, lava samples at Cordón Caulle do not appear to host direct or unambiguous evidence for a sintering origin; this is unsurprising given the large overprinting shear strains associated with lava out-flow and sub-aerial emplacement. This makes the obsidian pyroclasts and volcanic bombs at Cordón Caulle a better record of in-conduit processes simply because they did not experience the same shear strain during extrusion, and the fact that they

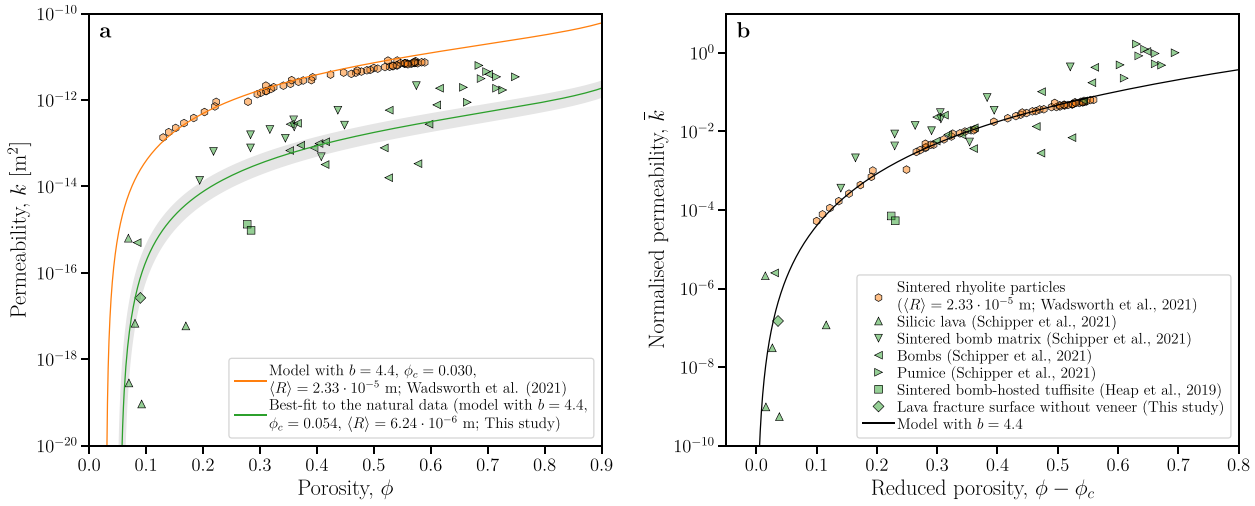

Fig. 16. Compilation of available permeability data for the 2011–2012 Cordón Caulle erupted products, compared with a theoretical model for permeability during sintering (Wadsworth et al., 2016b, 2017a, 2021b). Here we report data for the lava (this study and Schipper et al. (2021)), the bombs, and pumice Schipper et al. (2021), and tuffisites found within bombs (Heap et al., 2019). We additionally show data that results from experimentally sintered dense silicic (obsidian) particles in the size range pertinent to the bomb sintering (Fig. 12; Wadsworth et al. (2021a, 2021b)). We find a good match between the compiled data and the model, for a global particle size between 5 and 35 μm, consistent with the broad range of sizes found between the lava veneers and the bomb matrix particles (Fig. 12). (a) Dimensional result $k(\phi)$ with $\phi_c = 0.03$. (b) Dimensionless result found by applying the normalisation $\bar{k} = ks^2/[2(1-(\phi-\phi_c))]$ and the porosity reduction $\phi - \phi_c$, demonstrating that the natural and experimental data are obeying the same sintering-induced pore geometry changes, and that the data offset observed in (a) is due only to the different initial particle sizes.

are co-erupted in hybrid behaviour underpins our model. Manley (1995) noted the same key similarities between rhyolite lavas and welded ignimbrites and showed that, despite large shear strains, there are indeed textures diagnostic of welding. Nevertheless, Manley (1995) interpreted these as forming during flow over the surface via welding of the products of surface brecciation of lava, rather forming in the conduit. Indeed, Manley (1995) cautioned against the interpreting rhyolite lavas as the product of pyroclastic welding. Our model revisits that and we propose that rhyolite lavas can be considered an in-conduit, subsurface version of well-studied lava-like ignimbrites.

In general, welding, or sintering, is a process by which particles coalesce with one another in a complex 3D manner, expelling the gas from between the particles, and resulting in a denser, almost pore-free material. When the particles are effectively silicate melt droplets – i.e. low crystallinity, high temperature ash fragments that are above the glass transition interval – this process is typically rate-limited by the viscosity of the droplets and driven by both the interfacial tension at the pore-melt interfaces (Vasseur et al., 2013; Wadsworth et al., 2014, 2016a; Gardner et al., 2018, 2019) and any effective pressure acting on the droplets themselves (Wadsworth et al., 2019, 2021b). Complexities arise associated with the diffusive loss of H_2O into the pore phase during sintering, which can act to retard sintering rates (Wadsworth et al., 2019, 2021b). Wadsworth et al. (2020a) showed that, when the diffusive losses are accounted for during transport of pyroclasts up through the conduit, ultra-fines, such as those associated with the in-lava fracture veneers (Farquharson et al., 2022), can degas to equilibrium, raising their viscosity and potentially slowing the sintering process. Nevertheless, because these particles are so small, Wadsworth et al. (2020a) found that they still sinter more quickly than larger pyroclast fractions. This implies that sintering of ultra-fines in the shallow conduit can be effective and rapid.

Deeper in the conduit, the H_2O partial pressures will presumably be elevated, and so it is likely that particles captured deeper, being relatively more hydrous, will sinter with a lower viscosity, and therefore more rapidly. Any particle–particle pressures applied by closing the fractures in between intermittent ash venting will act to accelerate this process (Wadsworth et al., 2019). Therefore, in line with previous work, we conclude that sintering is a tenable process for lava assembly on the timescales of lava extrusion (Castro et al., 2014; Wadsworth et al., 2020a; Schipper et al., 2021).

The equilibrium porosity – or gas volume fraction – at the end of sintering of monodisperse spherical particles is 0.03 (Wadsworth et al., 2016a), consistent with geometric evidence from packs of spheres (Kertesz, 1981; Rintoul, 2000; Vasseur and Wadsworth, 2017). This porosity (which can be thought of as the 'post-sintering trapped pore phase') is slightly higher in the case of angular particles (Wadsworth et al., 2016b; Reis et al., 2018) and slightly lower in the case of polydisperse particles (Prado et al., 2003; Wadsworth et al., 2017b). These differences from the 0.03 value are maximally of the order of ±0.03. Given that many of the obsidian pyroclasts analysed here and elsewhere (Gardner et al., 2017, 2019) are non-porous or within the range 0–0.06 porosity, this, along with the direct textural evidence, is consistent with a sinter-formation mechanism. However, much of the lava itself has porosities higher than this low range. While there are indeed dense obsidian-like portions of the Cordón Caulle lava, much of it has moderate porosity, well above 0.03 (Schipper et al., 2019, 2021). This can be explained through secondary degassing into the post-sintering trapped pore phase upon lava extrusion (see the explanation of finely vesicular pumice; Manley and Fink, 1987). Modest secondary degassing can result in a relatively large change in bulk porosity (Fink et al., 1992). For example, if degassing were to occur at 0.11 wt% H_2O, and the lava were subsequently extruded such that the equilibrium H_2O falls to 0.1 wt%, then complete degassing to equilibrium would raise the residual porosity from 0.03 to 0.5. This change in H_2O concentration effectively equates to the very final pressure change in the final meter or so of ascent to the surface (assuming 2000 kgm^{-3} density, 1000 K temperature, and the Liu et al. (2005) solubility model). This, in turn, suggests that secondary degassing processes are likely to be highly effective in modulating the final porosity of the deposit, blurring the distinction between a non-fragmental magmatic evolution and a clastogenic textural evolution (Schipper et al., 2021) and even causing portions of the lava to become pumiceous (Manley and Fink, 1987; Fink et al., 1992).

We have not made a thorough textural investigation of the lava itself in this study, except in the vicinity of lava fracture surfaces. However, there are internal features of lavas studied elsewhere that appear to be

texturally consistent with a sintering origin, despite the large shear-strains that occur during sub-aerial emplacement. To illustrate this, in Fig. 17, we juxtapose two types of image: (1) a published image of 'coarsely vesicular pumice' found in a lava core (~35 m from the base of a 55 m-thick lava at Obsidian Dome but well below the 'finely vesicular pumice' lava flow top) with approximately 22 vol% porosity (from Manley and Fink, 1987); and (2) two 2D slices through a 3D x-ray computed tomography dataset from the middle of a sample of partially sintered obsidian ash-sized particles (from Wadsworth et al., 2019). There is a striking textural similarity between these two images, and while not strictly diagnostic, we propose that this textural similarity supports our model. The lack of shear-induced overprint here is perhaps because the drilling from which Fig. 17a was taken is relatively vent-proximal. Additionally, rafting and strain localization in silicic lavas is poorly understood, such that the vertical stratigraphy may generally be varied (Fink, 1983; Manley and Fink, 1987). We do not propose that in-lava textural similarities are themselves the key evidence here, but, in concert with our proposed reconstruction of the in-conduit processes, componentry, geometries, and rates, this textural evidence that comes directly from lava is compelling.

Sintering involves the discrete transition from open and permeable porosity to isolated porosity (Wadsworth et al., 2017a, 2021b). In the model that we propose, this transition can occur at a shallow depth in the conduit, which solves a conundrum identified by previous workers (Taylor et al., 1983; Eichelberger et al., 1986; Castro et al., 2014) – that dominantly open-system degassing hydrogen-isotope systematics are associated with silicic lavas that have low or zero final permeability. Similarly, this transition is key to the process of cristobalite formation in isolated pores, divorcing the origin of the acidic fluids necessary for the corrosion and silica-leaching processes of the groundmass (Fig. 7) from the melt surrounding the pores, and opening the possibility that the fluids are sourced from depth and the through-fluxing gas phases instead (Horwell et al., 2013), then trapped.

9.2. *Implications for shallow laccolith emplacement within the pyroclastic hybrid framework*

Uplift patterns around the vent during the explosive and hybrid eruptive behaviour at the 2011–2012 Cordón Caulle eruption are associated with up to 0.8 km^3 of volume change, and have been attributed to emplacement of a shallow laccolith body (Castro et al., 2016). In order to explain the lateral intrusion and uplift quantitatively, Castro et al. (2016) invoked shallow conduit constriction. This was shown to be able to cause sufficient conduit pressure increase to laterally fracture the country rock and allow magma intrusion. Such a conduit constriction, which coincided with the onset of intense bomb-forming explosions, is consistent with our model, in which shallow conduit blockage arises from sintering-driven lava assembly. Lateral gas-driven hydrofracturing would be the dominant mechanism of lateral fracture formation above fragmentation, followed by injection of magmatic particle proppant, similar to the model by Unwin et al. (2021) for lateral injection of a pyroclastic sill.

Zheng et al. (2020) analyse synthetic aperture radar imagery and data over the period June 2011 to March 2012, and find that over 200 m uplift occurred in that 9-month period (Zheng et al., 2020; Lobos et al., 2021). Importantly, the initial uplift preceded the appearance of lava at the vent (first identified by Castro et al., 2016). They report that uplift was the dominant deformation signal until mid-July 2011, when a subsidence signal was recorded, confirmed by digital elevation models, showing 40 m elevation loss from August 2011. They conclude that magma must have migrated out of the laccolith to explain the subsidence. Instead, we propose that, if the hydrofracture into the laterally growing intrusion was dominantly pyroclastic, similar to known field examples of intrusions around dissected rhyolitic conduits (Heiken et al., 1988; Unwin et al., 2021), then the subsidence can be explained by the sintering of the pyroclasts in the growing clastic intrusion. By its nature, such sintering involves up to 45% volume loss (Wadsworth et al., 2019).

In Fig. 13, we depict a conceptualized model architecture for the 2011–2012 Cordón Caulle system, including a shallow intrusion drawn at or immediately above the arbitrarily depicted shallow fragmentation depth. Unwin et al. (2021) show that lateral hydrofractures can open in country rock at elevated conduit pressures at or immediately above fragmentation. We suggest that it is possible that laccolith emplacement is part of a continuum that includes pyroclastic sill emplacement, external tuffisite dynamics, and inflating laccoliths. External tuffisites are typically inferred to originate in a conduit source filled with coherent liquid magma or relatively thin conduit-marginal breccia (Stasiuk et al., 1996; Kolzenburg et al., 2019; Davies et al., 2021; Heap et al., 2021) or as a vanguard fragmental magma that proceeds ahead of the emplacement of dense magma (Saubin et al., 2019). Our model suggests a different origin – that they are instead associated with gas-driven fracking (Stasiuk et al., 1996; Saubin et al., 2019) and that the juxtaposed dense magma deposits may themselves be sintered from the clastic emplacement, in contrast with previous models (Saubin et al., 2019). In Fig. 13, we do not attempt to depict the wholly unknown geometry of laccolith emplacement at Cordón Caulle, however, we do invoke supra-fragmentation hydrofracture-driven injection as a plausible mechanism for the opening of a sub-surface intrusive pathway. If the emplacement is supra-fragmentation, then the medium doing mechanical work on the country rock is a highly compressible gas-pyroclast dispersion, rather than coherent, unfragmented and broadly

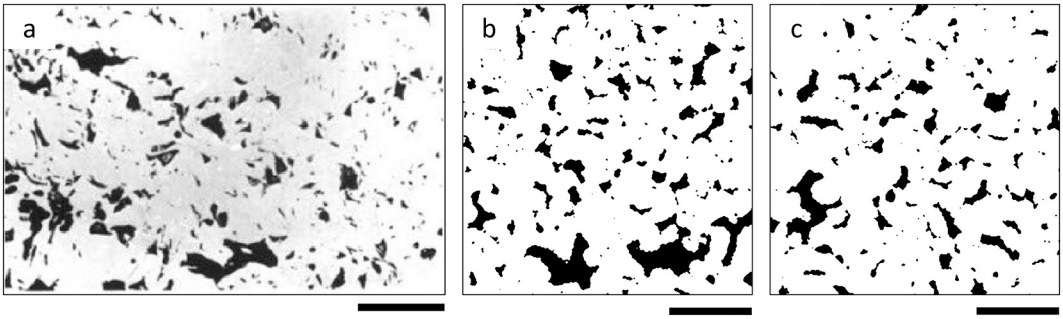

Fig. 17. A comparison of internal textures in silicic lava and sintered silicic obsidian particles. (a) A sample from the RDO-2A core through Obsidian Dome from ~35 m from the base of the locally 55 m-thick lava in material denoted 'coarsely vesicular pumice' (Manley and Fink, 1987). (b-c) Segmented 2D slices through a 3D tomography dataset showing obsidian particles part-way through the sintering process (Wadsworth et al., 2019). The samples in all images are at 20–22 vol% porosity. The proposal here is that shear-deformation during sustained lava flow would overprint the texture in (a) and obscure primary apparent sintering textures. The scale bar in (a) is 1 mm (Manley and Fink, 1987) and in (b-c) is 0.1 mm (Wadsworth et al., 2019); we note that sintering textures scale with the component particle sizes, such that if the image in (a) has a sintering genesis, then the particles involved would be coarser than those used in (b) and (c). See Wadsworth et al. (2019) for the particle sizes used to produce the data shown in (b) and (c).

incompressible magma.

9.3. Implications for geophysics and unrest associated with hybrid behaviour

Prior to the onset of the Cordón Caulle eruption, seismic unrest in February 2011 was characterised by volcano-tectonic, long-period, and hybrid earthquakes, which shallowed and intensified in April 2011. On 3 June 2011, just prior to eruption on 4 June 2011, earthquake epicentres moved to the ultimate vent area and further shallowed toward the surface. From 15 June 2011, quasi-harmonic tremor was recorded (Bertin et al., 2015). Such tremor can be explained by superimposed long-period events associated with resonating, jerky advance of pressurized cracks (Chouet, 1988, 1996), with models recently modified to include injection of gas and particles into gas pockets trapped beneath plugs of permeable lava blocking the shallow conduit (Traphagan and Lees, 2020). The crack resonance models of Kumagai and Chouet (2000) required 'dusty' or 'misty' fluids, such that they are laden with micron-scale particles, in order to explain the measured quality factor of LP seismicity at Galeras, Columbia. We note that 15 June seismic activity—characterised by a strong component of quasi-harmonic tremor (Bertin et al., 2015)—corresponds closely in time to the observed onset of hybrid behaviour, defined as the first observation of lava emission from the vent area. This evidence links the transition to hybrid explosive–effusive behaviour to the processes generating quasi-harmonic tremor. These observations and constraints are entirely consistent with our model. The explosive portion of the hybrid behaviour is associated with jerky and intermittent (Schipper et al., 2013) through-lava fracture clearing of a dusty, ash-laden fluid, consistent with models of the origin of long-period events (Chouet, 1988, 1996). The gas is dusty, which is consistent with models for volcanic tremor (Kumagai and Chouet, 2000; Traphagan and Lees, 2020) and the micron-scale particles required in those models match the grainsize of the particles sintered to the in-lava fracture surfaces. We therefore emphasise that volcanic tremor and hybrid behaviour may be genetically linked, and our model then provides further insight into the nature of the seismic source.

9.4. Comparison with basaltic hybrid eruptive behaviour

Hybrid eruption of both tephra-rich plumes and effusive lavas from the same vent, or closely-associated vents, is common at basaltic volcanoes (Cioni et al., 2008; Pioli et al., 2008, 2009; Wadsworth et al., 2022; Pankhurst et al., 2022). However, it is likely that basaltic hybrid behaviour results from different processes from those we propose for the silicic counterpart. In the basaltic case, it is likely that hybrid eruption results from the well-established behaviour of decoupled bubbles (Gonnermann and Manga, 2013; Pioli et al., 2017). Gas decoupling provides a mechanism for hybrid explosive-effusive behaviour, in which the gas-rich component erupts explosively, while the gas-poor component erupts effusively. This mechanism is not feasible in high viscosity silicic magma. Nevertheless, the identification of mafic end-member versions of tuffisites (Owen et al., 2019) and fracture-healing textures in explosive deposits (Taddeucci et al., 2021) suggests that there may be some similarities in process across the compositional spectrum of magmas, that may lead to some generalization of hybrid eruption dynamics. Indeed, it is common for basaltic lavas to form clastogenically from fountaining behaviour at basaltic eruptions (Sumner, 1998). Clastogenic lava assembly in basalts is typically envisaged as occurring sub-aerially as the products of fountaining land and agglutinate by low-viscosity sintering on the Earth's surface. Here, we propose that in the silicic case, this is common in-conduit in the shallow sub-surface.

10. Conclusions and outlook

Previous models for hybrid silicic eruptions have generally treated explosive, effusive, and intrusive activity as separate. In particular, explosive phases have been attributed to periods of magma fragmentation, whereas effusive phases have been attributed to periods when coherent magma reaches the vent without wholesale fragmentation. We propose a model in which explosive, apparently effusive, and hybrid activity are part of a continuum, in which shifts in style arise from variable occlusion of the shallow conduit by sintering of clastic products of sustained fragmentation at depth. This model further attributes syn-eruptive laccolith intrusion to large-scale hydro-fracturing of the country rock by pressurized dusty gas beneath the sintered plug. The conceptual model is summarized in Fig. 13.

The model resolves a number of apparently paradoxical or surprising observations. Shallow sintering of fine clastic products explains why effusive products are thoroughly outgassed but have low permeability, and why hydrogen isotopic evidence shows open-system degassing in effused lavas. Transient fracturing of the occluding plug by pressurized gas within the underlying conduit explains the origin of prolonged hybrid activity. Rubbly, clastic conduit infill explains complex textures of bombs, and the presence of a dusty gas phase in the conduit explains the origin of harmonic seismic tremor. It will be important to understand the temperatures of such a clast-supported conduit-filling rubble, as well as the contact times and interaction dynamics between through-going fragmental particles and sintering surfaces, if the spatial distribution of sintering timescales, and therefore the evolving plug geometries, are to be known in 3D.

The model directly connects explosive, apparently effusive, and syn-eruptive intrusive behaviour to persistent gas-and-ash reservoirs in the shallow subsurface. Ultimately this possibility suggests that quantitative models of magma ascent, which predict that effusive lava is produced when the conditions of fragmentation (e.g., ascent rate, gas content) are not met, require revisiting. Predictive models for explosive–effusive behaviour, in which the effusive phase is welded from the products of the explosive phase, should be coupled, accounting for the fact that welding-driven occlusion of the shallowest portions of the vent will feedback to the fragmentation process at depth below the assembling lava plug. Further work is required to address the 3D geometry of the shallow plumbing system at silicic volcanoes, the implications of the proposal that near-surface sintering drives laccolith emplacement and the onset of hybrid explosive–effusive behaviour, and the relationship between the evolution of an explosive–effusive eruption and its associated geophysical signals.

Data availability statement

All processed data are provided as supplementary data files.

CRediT authorship contribution statement

Fabian B. Wadsworth: Conceptualization, Methodology, Formal analysis, Writing – original draft, Visualization. **Edward W. Llewellin:** Conceptualization, Writing – review & editing. **Jonathan M. Castro:** Methodology, Investigation, Resources, Formal analysis, Writing – review & editing. **Hugh Tuffen:** Conceptualization, Writing – review & editing. **C. Ian Schipper:** Investigation, Resources, Writing – review & editing. **James E. Gardner:** Resources, Writing – review & editing. **Jérémie Vasseur:** Conceptualization, Formal analysis. **Annabelle Foster:** Conceptualization, Visualization, Writing – review & editing. **David E. Damby:** Investigation, Resources, Writing – review & editing. **Iona M. McIntosh:** Methodology, Resources, Formal analysis, Writing – review & editing. **Sina Boettcher:** Investigation, Resources, Formal analysis. **Holly E. Unwin:** Writing – review & editing. **Michael J. Heap:** Methodology, Investigation, Resources, Formal analysis, Writing – review & editing. **Jamie I. Farquharson:** Formal analysis, Writing – review & editing. **Donald B. Dingwell:** Writing – review & editing, Funding acquisition. **Kayla Iacovino:** Resources, Writing – review & editing. **Rebecca Paisley:** Investigation, Resources. **Calvin Jones:** Investigation, Resources. **Jack Whattam:** Investigation, Resources.

Declaration of Competing Interest

The authors declare that they have no known competing financial interests or personal relationships that could have appeared to influence the work reported in this paper.

Data availability

Data is available in the Supplementary Information

Acknowledgments

We are grateful to Mike James, Kim Berlo, Peter Sammonds, and Amy Chadderton, for discussion in the field, and to Shane Rooyakkers, Madeleine Humphreys, Yan Lavallée, Jackie Kendrick, Anthony Lamur, Joshua Weaver, and Bettina Scheu for broad discussion about silicic eruptions and eruption transitions in general. M. Heap acknowledges support from the Institut Universitaire de France (IUF). J. Gardner acknowledges support from NSF grant EAR–1852449. Funding was provided by ERC ADV 2009 no- 247076 EVOKES and ADV 2018 no. 834225 EAVESDROP (both to DBD, by the Natural Environment Research Council grants NE/N002954/1, NE/T007796/1, and by the Royal Society (URF to HT). The BBC are thanked for loan of camera equipment used to film the Cordón Caulle eruption in 2012. Any use of trade, firm, or product names is for descriptive purposes only and does not imply endorsement by the U.S. Government. Comments by Ben Ellis, one anonymous reviewer, and the USGS internal review team, all improved the manuscript. Editorial handling by Sonia Calvari is gratefully acknowledged.

Appendix A. Supplementary data

Supplementary data to this article can be found online at https://doi.org/10.1016/j.jvolgeores.2022.107672.

References

Adams, N.K., Houghton, B.F., Fagents, S.A., Hildreth, W., 2006. The transition from explosive to effusive eruptive regime: the example of the 1912 Novarupta eruption, Alaska. Bull. Geol. Soc. Am. 118, 620–634. https://doi.org/10.1130/B25768.1.

Alidibirov, M., Dingwell, D.B., 1996. Magma fragmentation by rapid decompression. Nature 380, 146–148. https://doi.org/10.1038/380146a0.

Andrews, G.D.M., Branney, M.J., 2011. Emplacement and rheomorphic deformation of a large, lava-like rhyolitic ignimbrite: grey's Landing, southern Idaho. Geol. Soc. Am. Bull. 123, 725–743. https://doi.org/10.1130/b30167.1.

Andrews, G.D.M., Kenderes, S.M., Whittington, A.G., et al., 2021. The fold illusion: the origins and implications of ogives on silicic lavas. Earth Planet. Sci. Lett. 553, 116643 https://doi.org/10.1016/j.epsl.2020.116643.

Behrens, H., Tamic, N., Holtz, F., 2004. Determination of the molar absorption coefficient for the infrared absorption band of CO2 in rhyolitic glasses. Am. Mineral. 89, 301–306. https://doi.org/10.2138/am-2004-2-307.

Berlo, K., Tuffen, H., Smith, V.C., et al., 2013. Element variations in rhyolitic magma resulting from gas transport. Geochim. Cosmochim. Acta 121, 436–451. https://doi.org/10.1016/j.gca.2013.07.032.

Bertin, D., Lara, L.E., Basualto, D., et al., 2015. High effusion rates of the Cordón Caulle 2011–2012 eruption (Southern Andes) and their relation with the quasi-harmonic tremor. Geophys. Res. Lett. 42, 7054–7063. https://doi.org/10.1002/2015GL064624.

Black, B.A., Manga, M., Andrews, B., 2016. Ash production and dispersal from sustained low-intensity Mono-Inyo eruptions. Bull. Volcanol. 78, 57. https://doi.org/10.1007/s00445-016-1053-0.

Bonadonna, C., Pistolesi, M., Cioni, R., et al., 2015. Dynamics of wind-affected volcanic plumes: the example of the 2011 Cordón Caulle eruption, Chile. J. Geophys. Res. Solid Earth 120, 2242–2261. https://doi.org/10.1002/2014JB011478.

Boyd, F.R., 1961. Welded tuffs and flows in the rhyolite plateau of Yellowstone Park, Wyoming. Geol. Soc. Am. Bull. 72, 387–426. https://doi.org/10.1130/0016-7606(1961)72.

Branney, M.J., Kokelaar, P., 1992. A reappraisal of ignimbrite emplacement: progressive aggradation and changes from particulate to non-particulate flow during emplacement of high-grade ignimbrite. Bull. Volcanol. 54, 504–520. https://doi.org/10.1007/BF00301396.

Branney, M.J., Kokelaar, B.P., 2002. Pyroclastic Density Currents and the Sedimentation of Ignimbrites. The Geological Society of London, London.

Branney, M.J., Kokelaar, B.P., McConnell, B., 1992. The Bad Step Tuff: a lava-like rheomorphic ignimbrite in a calc-alkaline piecemeal caldera, English Lake District. Bull. Volcanol. 54, 187–199. https://doi.org/10.1007/BF00278388.

Cabrera, A., Weinberg, R.F., Wright, H.M.N., 2015. Magma fracturing and degassing associated with obsidian formation: the explosive–effusive transition. J. Volcanol. Geotherm. Res. 298, 71–84. https://doi.org/10.1016/j.jvolgeores.2014.12.014.

Casas, A.S., Wadsworth, F.B., Ayris, P.M., et al., 2019. SO_2 scrubbing during percolation through rhyolitic volcanic domes. Geochim. Cosmochim. Acta. https://doi.org/10.1016/j.gca.2019.04.013.

Cassidy, M., Manga, M., Cashman, K., Bachmann, O., 2018. Controls on explosive-effusive volcanic eruption styles. Nat. Commun. 9, 2839. https://doi.org/10.1038/s41467-018-05293-3.

Castro, J.M., Dingwell, D.B., 2009. Rapid ascent of rhyolitic magma at Chaitén volcano, Chile. Nature 461, 780–783. https://doi.org/10.1038/nature08458.

Castro, J.M., Gardner, J.E., 2008. Did magma ascent rate control the explosive-effusive transition at the Inyo volcanic chain, California? Geology 36, 279–282. https://doi.org/10.1130/G24453A.1.

Castro, J.M., Cordonnier, B., Tuffen, H., et al., 2012. The role of melt-fracture degassing in defusing explosive rhyolite eruptions at volcán Chaitén. Earth Planet. Sci. Lett. 333–334, 63–69. https://doi.org/10.1016/j.epsl.2012.04.024.

Castro, J.M., Schipper, C.I., Mueller, S.P., et al., 2013. Storage and eruption of near-liquidus rhyolite magma at Cordón Caulle, Chile. Bull. Volcanol. 75, 702. https://doi.org/10.1007/s00445-013-0702-9.

Castro, J.M., Bindeman, I.N., Tuffen, H., Ian Schipper, C., 2014. Explosive origin of silicic lava: Textural and δD–H_2O evidence for pyroclastic degassing during rhyolite effusion. Earth Planet. Sci. Lett. 405, 52–61. https://doi.org/10.1016/j.epsl.2014.08.012.

Castro, J.M., Cordonnier, B., Schipper, C.I., et al., 2016. Rapid laccolith intrusion driven by explosive volcanic eruption. Nat. Commun. 7, 13585. https://doi.org/10.1038/ncomms13585.

Chouet, B., 1988. Resonance of a fluid-driven crack: radiation properties and implications for the source of long-period events and harmonic tremor. J. Geophys. Res. Solid Earth 93, 4375–4400. https://doi.org/10.1029/JB093iB05p04375.

Chouet, B.A., 1996. Long-period volcano seismicity: its source and use in eruption forecasting. Nature 380, 309–316. https://doi.org/10.1038/380309a0.

Cioni, R., Bertagnini, A., Santacroce, R., Andronico, D., 2008. Explosive activity and eruption scenarios at Somma-Vesuvius (Italy): towards a new classification scheme. J. Volcanol. Geotherm. Res. 178, 331–346. https://doi.org/10.1016/j.jvolgeores.2008.04.024.

Costa, A., Pioli, L., Bonadonna, C., 2016. Assessing tephra total grain-size distribution: insights from field data analysis. Earth Planet. Sci. Lett. 443, 90–107. https://doi.org/10.1016/j.epsl.2016.02.040.

Damby, D.E., 2012. From Dome to Disease: The Respiratory Toxicity of Volcanic Cristobalite. Durham University.

Davies, B.V., Brown, R.J., Barclay, J., et al., 2021. Rapid eruptive transitions from low to high intensity explosions and effusive activity: insights from textural analysis of a small-volume trachytic eruption, Ascension Island, South Atlantic. Bull. Volcanol. 83, 58. https://doi.org/10.1007/s00445-021-01480-1.

Degruyter, W., Bachmann, O., Burgisser, A., Manga, M., 2012. The effects of outgassing on the transition between effusive and explosive silicic eruptions. Earth Planet. Sci. Lett. 349, 161–170. https://doi.org/10.1016/j.epsl.2012.06.056.

Delgado, F., Kubanek, J., Anderson, K., et al., 2019. Physicochemical models of effusive rhyolitic eruptions constrained with InSAR and DEM data: a case study of the 2011-2012 Cordón Caulle eruption. Earth Planet. Sci. Lett. 524, 115736 https://doi.org/10.1016/j.epsl.2019.115736.

Delmelle, P., Wadsworth, F.B., Maters, E.C., Ayris, P.M., 2018. High temperature reactions between gases and ash particles in volcanic eruption plumes. Rev. Mineral. Geochem. 84, 285–308. https://doi.org/10.2138/RMG.2018.84.8.

Dingwell, D.B., 1996. Volcanic dilemma: flow or blow? Science 273, 1054–1055. https://doi.org/10.1126/science.273.5278.1054.

Dingwell, D.B., Lavallée, Y., Hess, K.-U., et al., 2016. Eruptive shearing of tube pumice: pure and simple. Solid Earth 7, 1383–1393. https://doi.org/10.5194/se-7-1383-2016.

Dufek, J., Manga, M., Patel, A., 2012. Granular disruption during explosive volcanic eruptions. Nat. Geosci. 5, 561–564.

Eichelberger, J.C., Carrigan, C.R., Westrich, H.R., Price, R.H., 1986. Non-explosive silicic volcanism. Nature 323, 598–602. https://doi.org/10.1038/323598a0.

Elissondo, M., Baumann, V., Bonadonna, C., et al., 2016. Chronology and impact of the 2011 Cordón Caulle eruption, Chile. Nat. Hazards Earth Syst. Sci. 16, 675–704. https://doi.org/10.5194/nhess-16-675-2016.

Farquharson, J.I., James, M.R., Tuffen, H., 2015. Examining rhyolite lava flow dynamics through photo-based 3D reconstructions of the 2011–2012 lava flowfield at Cordón-Caulle, Chile. J. Volcanol. Geotherm. Res. 304, 336–348. https://doi.org/10.1016/j.jvolgeores.2015.09.004.

Farquharson, J.I., Wadsworth, F.B., Heap, M.J., Baud, P., 2017. Time-dependent permeability evolution in compacting volcanic fracture systems and implications for gas overpressure. J. Volcanol. Geotherm. Res. 339, 81–97. https://doi.org/10.1016/j.jvolgeores.2017.04.025.

Farquharson, J., Tuffen, H., Wadsworth, F., et al., 2022. In-conduit capture of sub-micron volcanic ash particles via turbophoresis and sintering. Nat. Commun. https://doi.org/10.21203/rs.3.rs-1152244/v1.

Fink, J.H., 1983. Structure and emplacement of a rhyolitic obsidian flow: Little Glass Mountain, Medicine Lake Highland, northern California. Geol. Soc. Am. Bull. 94, 362–380.

Fink, J.H., Anderson, S.W., Manley, C.R., 1992. Textural constraints on effusive silicic volcanism: beyond the permeable foam model. J. Geophys. Res. Solid Earth 97, 9073–9083. https://doi.org/10.1029/92JB00416.
Fowler, A.C., Scheu, B., 2016. A theoretical explanation of grain size distributions in explosive rock fragmentation. Proc. R Soc. A Math Phys. Eng. Sci. 472, 20150843. https://doi.org/10.1098/rspa.2015.0843.
Gardner, J.E., Llewellin, E.W., Watkins, J.M., Befus, K.S., 2017. Formation of obsidian pyroclasts by sintering of ash particles in the volcanic conduit. Earth Planet. Sci. Lett. 459, 252–263. https://doi.org/10.1016/J.EPSL.2016.11.037.
Gardner, J.E., Wadsworth, F.B., Llewellin, E.W., et al., 2018. Experimental sintering of ash at conduit conditions and implications for the longevity of tuffisites. Bull. Volcanol. 80, 23. https://doi.org/10.1007/s00445-018-1202-8.
Gardner, J.E., Wadsworth, F.B., Llewellin, E.W., et al., 2019. Experimental constraints on the textures and origin of obsidian pyroclasts. Bull. Volcanol. 81, 22. https://doi.org/10.1007/s00445-019-1283-z.
Giachetti, T., Gonnermann, H.M., Gardner, J.E., et al., 2015. Discriminating secondary from magmatic water in rhyolitic matrix-glass of volcanic pyroclasts using thermogravimetric analysis. Geochim. Cosmochim. Acta 148, 457–476. https://doi.org/10.1016/j.gca.2014.10.017.
Giachetti, T., Trafton, K.R., Wiejaczka, J., et al., 2021. The products of primary magma fragmentation finally revealed by pumice agglomerates. Geology 49, 1307–1311. https://doi.org/10.1130/G48902.1.
Gilbert, D.J., 2012. Pre-Eruptive Conditions at Lonquimay and Puyehue-Cordón Caulle Volcanoes. Framework for tectonic influences. Kiel University, Chile.
Gonnermann, H.M., Manga, M., 2005a. Flow banding in obsidian: a record of evolving textural heterogeneity during magma deformation. Earth Planet. Sci. Lett. 236, 135–147. https://doi.org/10.1016/j.epsl.2005.04.031.
Gonnermann, H.M., Manga, M., 2005b. Nonequilibrium magma degassing: results from modeling of the ca. 1340 A.D. eruption of Mono Craters, California. Earth Planet. Sci. Lett. 238, 1–16. https://doi.org/10.1016/j.epsl.2005.07.021.
Gonnermann, H.M., Manga, M., 2013. Dynamics of magma ascent in the volcanic conduit. In: Fagents, S.A., Gregg, T.K.P., Lopes, R.M.C. (Eds.), Modeling Volcanic Processes. Cambridge University Press, p. 421.
Heap, M.J., Farquharson, J.I., Wadsworth, F.B., et al., 2015. Timescales for permeability reduction and strength recovery in densifying magma. Earth Planet. Sci. Lett. 429, 223–233. https://doi.org/10.1016/j.epsl.2015.07.053.
Heap, M.J., Kushnir, A.R.L., Gilg, H.A., et al., 2017. Microstructural and petrophysical properties of the Permo-Triassic sandstones (Buntsandstein) from the Soultz-sous-Forêts geothermal site (France). Geotherm. Energy 5, 26. https://doi.org/10.1186/s40517-017-0085-9.
Heap, M.J., Tuffen, H., Wadsworth, F.B., et al., 2019. The permeability evolution of tuffisites and implications for outgassing through dense rhyolitic magma. J. Geophys. Res. Solid Earth 124, 8281–8299. https://doi.org/10.1029/2018jb017035.
Heap, M.J., Baumann, T., Gilg, H.A., et al., 2021. Hydrothermal alteration can result in pore pressurization and volcano instability. Geology 2021. https://doi.org/10.1130/G49063.1.
Heiken, G., Wohletz, K., Eichelberger, J., 1988. Fracture fillings and intrusive pyroclasts, Inyo Domes, California. J. Geophys. Res. Solid Earth 93, 4335–4350. https://doi.org/10.1029/JB093iB05p04335.
Hervig, R.L., Dunbar, N., Westrich, H.R., Kyle, P.R., 1989. Pre-eruptive water content of rhyolitic magmas as determined by ion microprobe analyses of melt inclusions in phenocrysts. J. Volcanol. Geotherm. Res. 36, 293–302. https://doi.org/10.1016/0377-0273(89)90075-9.
Horwell, C.J., Williamson, B.J., Llewellin, E.W., et al., 2013. The nature and formation of cristobalite at the Soufrière Hills volcano, Montserrat: implications for the petrology and stability of silicic lava domes. Bull. Volcanol. 75, 1–19.
Iddings, J., 1888. Obsidian Cliff, Yellowstone National Park. US GEol Surv Seventh Ann Rep, pp. 249–295.
Iddings, J., 1899. The rhyolites. In: Geology of the Yellowstone National Park. US Geological Survey, pp. 356–432.
Jaupart, C., Allègre, C.J., 1991. Gas content, eruption rate and instabilities of eruption regime in silicic volcanoes. Earth Planet. Sci. Lett. 102, 413–429. https://doi.org/10.1016/0012-821X(91)90032-D.
Jay, J., Costa, F., Pritchard, M., et al., 2014. Locating magma reservoirs using InSAR and petrology before and during the 2011–2012 Cordón Caulle silicic eruption. Earth Planet. Sci. Lett. 395, 254–266. https://doi.org/10.1016/j.epsl.2014.03.046.
Kertesz, J., 1981. Percolation of holes between overlapping spheres: Monte Carlo calculation of the critical volume fraction. J. Phys. Lett. 42, 393–395.
Kolzenburg, S., Ryan, A.G., Russell, J.K., 2019. Permeability evolution during non-isothermal compaction in volcanic conduits and tuffisite veins: implications for pressure monitoring of volcanic edifices. Earth Planet. Sci. Lett. 527, 115783 https://doi.org/10.1016/j.epsl.2019.115783.
Kueppers, U., Scheu, B., Spieler, O., Dingwell, D.B., 2006. Fragmentation efficiency of explosive volcanic eruptions: a study of experimentally generated pyroclasts. J. Volcanol. Geotherm. Res. 153, 125–135. https://doi.org/10.1016/j.jvolgeores.2005.08.006.
Kumagai, H., Chouet, B.A., 2000. Acoustic properties of a crack containing magmatic or hydrothermal fluids. J. Geophys. Res. Solid Earth 105, 25493–25512. https://doi.org/10.1029/2000JB900273.
Kushnir, A.R.L., Martel, C., Bourdier, J.L., et al., 2016. Probing permeability and microstructure: unravelling the role of a low-permeability dome on the explosivity of Merapi (Indonesia). J. Volcanol. Geotherm. Res. 316, 56–71. https://doi.org/10.1016/j.jvolgeores.2016.02.012.
Kushnir, A.R.L., Martel, C., Champallier, R., Wadsworth, F.B., 2017. Permeability evolution in variably glassy basaltic andesites measured under magmatic conditions. Geophys. Res. Lett. 44:10,210-262,271 https://doi.org/10.1002/2017GL074042.
Lara, L., 2010. The 2008 eruption of the Chaitén Volcano, Chile: a preliminary report. Andean Geol. 36, 125–130.
Lara, L.E., Naranjo, J.A., Moreno, H., 2004. Rhyodacitic fissure eruption in Southern Andes (Cordón Caulle; 40.5°S) after the 1960 (Mw:9.5) Chilean earthquake: a structural interpretation. J. Volcanol. Geotherm. Res. 138, 127–138. https://doi.org/10.1016/j.jvolgeores.2004.06.009.
Lavallee, Y., Wadsworth, F.B., Vasseur, J., et al., 2015. Eruption and emplacement timescales of ignimbrite super-eruptions from thermo-kinetics of glass shards. Front. Earth Sci. 3, 2. https://doi.org/10.3389/feart.2015.00002.
Liu, Y., Zhang, Y., Behrens, H., 2005. Solubility of H_2O in rhyolitic melts at low pressures and a new empirical model for mixed H_2O–CO_2 solubility in rhyolitic melts. J. Volcanol. Geotherm. Res. 143, 219–235.
Lobos, D.A., Delgado, F., Zheng, W., et al., 2021. Time-series of Laccolith evolution during and after the 2011-12 eruption of CordonCaulle volcano, Chile, from satellite feature-tracking, elevation, and thermal data. In: AGU, V35C-0142.
Magnall, N., James, M.R., Tuffen, H., Vye-Brown, C., 2017. Emplacing a cooling-limited rhyolite lava flow: similarities with basaltic lava flows. Front. Earth Sci. 5, 44.
Manley, C.R., 1995. How voluminous rhyolite lavas mimic rheomorphic ignimbrites: eruptive style, emplacement conditions, and formation of tuff-like textures. Geology 23, 349–352. https://doi.org/10.1130/0091-7613(1995)023<0349:HVRLMR>2.3.CO;2.
Manley, C.R., 1996. In situ formation of welded tuff-like textures in the carapace of a voluminous silicic lava flow, Owyhee County, SW Idaho. Bull. Volcanol. 57, 672–686. https://doi.org/10.1007/s004450050120.
Manley, C.R., Fink, J.H., 1987. Internal textures of rhyolite flows as revealed by research drilling. Geology 15, 549–552. https://doi.org/10.1130/0091-7613(1987)15<549:ITORFA>2.0.CO;2.
Manning, C.E., 1994. The solubility of quartz in H_2O in the lower crust and upper mantle. Geochim. Cosmochim. Acta 58, 4831–4839. https://doi.org/10.1016/0016-7037(94)90214-3.
Martel, C., Pichavant, M., Di Carlo, I., et al., 2021. Experimental constraints on the crystallization of silica phases in silicic magmas. J. Petrol. 62 (egab004) https://doi.org/10.1093/petrology/egab004.
Mastin, L.G., 2002. Insights into volcanic conduit flow from an open-source numerical model. Geochem. Geophys. Geosyst. 3, 1–18. https://doi.org/10.1029/2001GC000192.
McIntosh, I.M., Llewellin, E.W., Humphreys, M.C.S.S., et al., 2014. Distribution of dissolved water in magmatic glass records growth and resorption of bubbles. Earth Planet. Sci. Lett. 401, 1–11. https://doi.org/10.1016/j.epsl.2014.05.037.
McIntosh, I.M., Nichols, A.R.L., Tani, K., Llewellin, E.W., 2017. Accounting for the species-dependence of the 3500 cm−1 H2Ot infrared molar absorptivity coefficient: Implications for hydrated volcanic glasses. Am. Mineral. 102, 1677–1689. https://doi.org/10.2138/am-2017-5952CCBY.
Monnereau, L.R., Ellis, B.S., Szymanowski, D., et al., 2021. Obsidian pyroclasts in the Yellowstone-Snake River Plain ignimbrites are dominantly juvenile in origin. Bull. Volcanol. 83, 27. https://doi.org/10.1007/s00445-021-01448-1.
Newman, S., ES-A. Measurement of Water in Rhyolitic Glasses; Calibration of an Infrared Spectroscopic Technique. pubs.geoscienceworld.org undefined (1986).
Okumura, S., Nakashima, S., 2005. Molar absorptivities of OH and H_2O in rhyolitic glass at room temperature and at 400-600 °C. Am. Mineral. 90, 441–447. https://doi.org/10.2138/am.2005.1740.
Owen, J., Shea, T., Tuffen, H., 2019. Basalt, unveiling fluid-filled fractures, inducing sediment intra-void transport, ephemerally: examples from Katla 1918. J. Volcanol. Geotherm. Res. 369, 121–144. https://doi.org/10.1016/j.jvolgeores.2018.11.002.
Paisley, R., Berlo, K., Ghaleb, B., Tuffen, H., 2019a. Geochemical constraints on the role of tuffisite veins in degassing at the 2008–09 Chaitén and 2011–12 Cordón Caulle rhyolite eruptions. J. Volcanol. Geotherm. Res. 380, 80–93. https://doi.org/10.1016/j.jvolgeores.2019.05.013.
Paisley, R., Berlo, K., Whattam, J., et al., 2019b. Degassing-induced chemical heterogeneity at the 2011-2012 Cordón Caulle eruption. Volcanica 2, 211–237.
Pallister, J.S., Diefenbach, A.K., Burton, W.C., et al., 2013. The chaitén Rhyolite lava dome: eruption sequence, lava dome volumes, rapid effusion rates and source of the Rhyolite magma. Andean Geol. 40, 277–294. https://doi.org/10.5027/andgeoV40n2-a06.
Pankhurst, M.J., Scarrow, J.H., Barbee, O.A., et al., 2022. Rapid response petrology for the opening eruptive phase of the 2021 Cumbre Vieja eruption, La Palma, Canary Islands. Volcanica 5, 1–10. https://doi.org/10.30909/vol.05.01.0110.
Pioli, L., Erlund, E., Johnson, E., et al., 2008. Explosive dynamics of violent Strombolian eruptions: the eruption of Parícutin Volcano 1943–1952 (Mexico). Earth Planet. Sci. Lett. 271, 359–368. https://doi.org/10.1016/j.epsl.2008.04.026.
Pioli, L., Azzopardi, B.J., Cashman, K.V., 2009. Controls on the explosivity of scoria cone eruptions: magma segregation at conduit junctions. J. Volcanol. Geotherm. Res. 186, 407–415. https://doi.org/10.1016/j.jvolgeores.2009.07.014.
Pioli, L., Azzopardi, B.J., Bonadonna, C., et al., 2017. Outgassing and eruption of basaltic magmas: the effect of conduit geometry. Geology 45, 759–762. https://doi.org/10.1130/G38787.1.
Pistolesi, M., Cioni, R., Bonadonna, C., et al., 2015. Complex dynamics of small-moderate volcanic events: the example of the 2011 rhyolitic Cordón Caulle eruption, Chile. Bull. Volcanol. 77, 3. https://doi.org/10.1007/s00445-014-0898-3.
Prado, M.O., Zanotto, E.D., Fredericci, C., 2003. Sintering polydispersed spherical glass particles. J. Mater. Res. 18, 1347–1354.

Quane, S.L., Russell, J.K., 2005. Welding: insights from high-temperature analogue experiments. J. Volcanol. Geotherm. Res. 142, 67–87. https://doi.org/10.1016/j.jvolgeores.2004.10.014.

Reckziegel, F., Folch, A., Viramonte, J., 2019. ATLAS-1.0: atmospheric Lagrangian dispersion model for tephra transport and deposition. Comput. Geosci. 131, 41–51. https://doi.org/10.1016/j.cageo.2019.05.008.

Reis, R.M.C.V., Barbosa, A.J., Ghussn, L., et al., 2018. Sintering and rounding kinetics of irregular glass particles. J. Am. Ceram. Soc. 102 https://doi.org/10.1111/jace.15997.

Rintoul, M.D., 2000. Precise determination of the void percolation threshold for two distributions of overlapping spheres. Phys. Rev. E 62, 68.

Rust, A.C., Cashman, K.V., 2007. Multiple origins of obsidian pyroclasts and implications for changes in the dynamics of the 1300 B.P. eruption of Newberry Volcano, USA. Bull. Volcanol. 69, 825–845. https://doi.org/10.1007/s00445-006-0111-4.

Rust, A.C., Cashman, K.V., Wallace, P.J., 2004. Magma degassing buffered by vapor flow through brecciated conduit margins. Geology 32, 349–352. https://doi.org/10.1130/G20388.2.

Saubin, E., Tuffen, H., Gurioli, L., et al., 2016. Conduit dynamics in transitional rhyolitic activity recorded by tuffisite vein textures from the 2008–2009 Chaitén eruption. Front. Earth Sci. 4, 59.

Saubin, E., Kennedy, B., Tuffen, H., et al., 2019. Comparative field study of shallow rhyolite intrusions in Iceland: emplacement mechanisms and impact on country rocks. J. Volcanol. Geotherm. Res. 388, 106691 https://doi.org/10.1016/j.jvolgeores.2019.106691.

Schipper, C.I., Castro, J.M., Tuffen, H., et al., 2013. Shallow vent architecture during hybrid explosive–effusive activity at Cordón Caulle (Chile, 2011–12): evidence from direct observations and pyroclast textures. J. Volcanol. Geotherm. Res. 262, 25–37. https://doi.org/10.1016/j.jvolgeores.2013.06.005.

Schipper, C.I., Castro, J.M., Tuffen, H., et al., 2015. Cristobalite in the 2011–2012 Cordón Caulle eruption (Chile). Bull. Volcanol. 77, 34. https://doi.org/10.1007/s00445-015-0925-z.

Schipper, C.I., Castro, J.M., Kennedy, B.M., et al., 2019. Halogen (Cl, F) release during explosive, effusive, and intrusive phases of the 2011 rhyolitic eruption at Cordón Caulle volcano (Chile). Volcanica 2, 73–90. https://doi.org/10.30909/vol.02.01.7390.

Schipper, C.I., Rickard, W.D.A., Reddy, S.M., et al., 2020. Volcanic SiO_2-cristobalite: a natural product of chemical vapor deposition. Am. Mineral. 105, 510–524. https://doi.org/10.2138/AM-2020-7236.

Schipper, C.I., Castro, J.M., Kennedy, B.M., et al., 2021. Silicic conduits as supersized tuffisites: clastogenic influences on shifting eruption styles at Cordón Caulle volcano (Chile). Bull. Volcanol. 83, 11. https://doi.org/10.1007/s00445-020-01432-1.

Shields, J.K., Mader, H.M., Caricchi, L., et al., 2016. Unravelling textural heterogeneity in obsidian: shear-induced outgassing in the Rocche Rosse flow. J. Volcanol. Geotherm. Res. 310, 137–158. https://doi.org/10.1016/j.jvolgeores.2015.12.003.

Silva Parejas, C., Lara, L.E., Bertin, D., et al., 2012. The 2011–2012 eruption of Cordón Caulle volcano (Southern Andes): Evolution, crisis management and current hazards. In: EGU General Assembly Conference Abstracts, p. 9382.

Sparks, R.S.J., Stasiuk, M.V., Gardeweg, M., Swanson, D.A., 1993. Welded breccias in andesite lavas. J. Geol. Soc. Lond. 150, 897–902. https://doi.org/10.1144/gsjgs.150.5.0897.

Stasiuk, M.V., Barclay, J., Carroll, M.R., et al., 1996. Degassing during magma ascent in the Mule Creek vent (USA). Bull. Volcanol. 58, 117–130.

Stolper, E., 1982. Water in silicate glasses: an infrared spectroscopic study. Contrib. Mineral. Petrol. 81, 1–17. https://doi.org/10.1007/BF00371154.

Sumner, J.M., 1998. Formation of clastogenic lava flows during fissure eruption and scoria cone collapse: the 1986 eruption of Izu-Oshima Volcano, eastern Japan. Bull. Volcanol. 60, 195–212. https://doi.org/10.1007/s004450050227.

Taddeucci, J., Cimarelli, C., Alatorre-Ibargüengoitia, M.A., et al., 2021. Fracturing and healing of basaltic magmas during explosive volcanic eruptions. Nat. Geosci. 14, 248–254. https://doi.org/10.1038/s41561-021-00708-1.

Taylor, B.E., Eichelberger, J.C., Westrich, H.R., 1983. Hydrogen isotopic evidence of rhyolitic magma degassing during shallow intrusion and eruption. Nature 306, 541–545. https://doi.org/10.1038/306541a0.

Traphagan, J., Lees, J., 2020. Modeling source parameters of quasi-periodic tremor. Volcanica 3, 251–262. https://doi.org/10.30909/vol.03.02.251262.

Tuffen, H., Castro, J.M., 2009. The emplacement of an obsidian dyke through thin ice: Hrafntinnuhryggur, Krafla Iceland. J. Volcanol. Geotherm. Res. 185, 352–366.

Tuffen, H., Dingwell, D., 2005. Fault textures in volcanic conduits: evidence for seismic trigger mechanisms during silicic eruptions. Bull. Volcanol. 67, 370–387. https://doi.org/10.1007/s00445-004-0383-5.

Tuffen, H., Dingwell, D.B., Pinkerton, H., 2003. Repeated fracture and healing of silicic magma generate flow banding and earthquakes? Geology 31, 1089–1092. https://doi.org/10.1130/g19777.1.

Tuffen, H., James, M.R., Castro, J.M., Schipper, C.I., 2013. Exceptional mobility of an advancing rhyolitic obsidian flow at Cordón Caulle volcano in Chile. Nat. Commun. 4, 2709. https://doi.org/10.1038/ncomms3709.

Unwin, H.E., Tuffen, H., Phillips, E., et al., 2021. Pressure-driven opening and filling of a volcanic hydrofracture recorded by tuffisite at Húsafell, Iceland: a potential seismic source. Front. Earth Sci. 9, 347.

Vasseur, J., Wadsworth, F.B., 2017. Sphere models for pore geometry and fluid permeability in heterogeneous magmas. Bull. Volcanol. 79, 77. https://doi.org/10.1007/s00445-017-1165-1.

Vasseur, J., Wadsworth, F.B., Lavallée, Y., et al., 2013. Volcanic sintering: timescales of viscous densification and strength recovery. Geophys. Res. Lett. 40, 5658–5664. https://doi.org/10.1002/2013GL058105.

von Aulock, F.W., Kennedy, B.M., Maksimenko, A., et al., 2017. Outgassing from open and closed magma foams. Front. Earth Sci. 5 https://doi.org/10.3389/feart.2017.00046.

Wadsworth, F.B., Vasseur, J., Aulock, F.W., et al., 2014. Nonisothermal viscous sintering of volcanic ash. J. Geophys. Res. Solid Earth 119, 8792–8804.

Wadsworth, F.B., Vasseur, J., Llewellin, E.W., et al., 2016a. Sintering of viscous droplets under surface tension. Proc. R Soc. A Math Phys. Eng. Sci. 472, 20150780. https://doi.org/10.1098/rspa.2015.0780.

Wadsworth, F.B., Vasseur, J., Scheu, B., et al., 2016b. Universal scaling of fluid permeability during volcanic welding and sediment diagenesis. Geology 44, 219–222. https://doi.org/10.1130/G37559.1.

Wadsworth, F.B., Vasseur, J., Llewellin, E.W., et al., 2017a. Topological inversions in coalescing granular media control fluid-flow regimes. Phys. Rev. E 96, 033113. https://doi.org/10.1103/PhysRevE.96.033113.

Wadsworth, F.B., Vasseur, J., Llewellin, E.W., Dingwell, D.B., 2017b. Sintering of polydisperse viscous droplets. Phys. Rev. E 95. https://doi.org/10.1103/PhysRevE.95.033114.

Wadsworth, F.B., Witcher, T., Vossen, C.E.J., et al., 2018. Combined effusive-explosive silicic volcanism straddles the multiphase viscous-to-brittle transition. Nat. Commun. 9, 1–8. https://doi.org/10.1038/s41467-018-07187-w.

Wadsworth, F.B., Vasseur, J., Schauroth, J., et al., 2019. A general model for welding of ash particles in volcanic systems validated using in situ X-ray tomography. Earth Planet. Sci. Lett. 525, 115726 https://doi.org/10.1016/j.epsl.2019.115726.

Wadsworth, F.B., Llewellin, E.W., Vasseur, J., et al., 2020a. Explosive-effusive volcanic eruption transitions caused by sintering. Sci. Adv. 6 https://doi.org/10.1126/sciadv.aba7940 eaba7940.

Wadsworth, F.B., Vossen, C.E.J., Schmid, D., et al., 2020b. Determination of permeability using a classic Darcy water column. Am. J. Phys. 88, 20–24. https://doi.org/10.1119/10.0000296.

Wadsworth, F., Vasseur, J., Casas, A., et al., 2021a. A model for the kinetics of high temperature reactions between polydisperse volcanic ash and SO_2 gas. Am. Mineral. https://doi.org/10.2138/am-2021-7691.

Wadsworth, F.B., Vasseur, J., Llewellin, E.W., et al., 2021b. A model for permeability evolution during volcanic welding. J. Volcanol. Geotherm. Res. 409, 107118 https://doi.org/10.1016/j.jvolgeores.2020.107118.

Wadsworth, F.B., Llewellin, E.W., Farquharson, J.I., et al., 2022. Crowd-sourcing observations of volcanic eruptions during the 2021 Fagradalsfjall and Cumbre Vieja events. Nat. Commun. 13, 2611. https://doi.org/10.1038/s41467-022-30333-4.

Wang, Y., Gardner, J.E., Hoblitt, R.P., 2021. Formation of dense pyroclasts by sintering of ash particles during the preclimactic eruptions of Mt. Pinatubo in 1991. Bull. Volcanol. 83, 6. https://doi.org/10.1007/s00445-020-01427-y.

Watkins, J.M., Gardner, J.E., Befus, K.S., 2017. Nonequilibrium degassing, regassing, and vapor fluxing in magmatic feeder systems. Geology 45, 183–186. https://doi.org/10.1130/G38501.1.

Westrich, H.R., Eichelberger, J.C., 1994. Gas transport and bubble collapse in rhyolitic magma: an experimental approach. Bull. Volcanol. 56, 447–458. https://doi.org/10.1007/BF00302826.

Wolff, J.A., 1986. Welded-tuff dykes, conduit closure, and lava dome growth at the end of explosive eruptions. J. Volcanol. Geotherm. Res. 28, 379–384. https://doi.org/10.1016/0377-0273(86)90032-6.

Woods, A.W., Koyaguchi, T., 1994. Transitions between explosive and effusive eruptions of silicic magmas. Nature 370, 641–644. https://doi.org/10.1038/370641a0.

Zhang, Y., Ni, H., 2010. Diffusion of H, C, and O components in silicate melts. Rev. Mineral. Geochem. 72, 171–225. https://doi.org/10.2138/rmg.2010.72.5.

Zheng, W., Pritchard, M.E., Delgado, F., et al., 2020. Laccolith evolution during and after the 2011-12 eruption of Cordon Caulle volcano, Chile, from satellite feature-tracking, elevation, and thermal observations. In: AGUFM 2020:V004–0025.